Granular Flow Experiments for Validation of Numerical Flow Models

Amy Webb and Marcus Bursik

This page intentionally left blank

Contents

List of Figures

List of Tables

Abstract

Many types of geophysical flows such as debris avalanches and pyroclastic flows pose significant danger to both people and property. Understanding granular avalanche behavior and particle interaction during the course of a flow is very important in the development of granular flow models. Since it is not always convenient or possible to use actual events to validate flow models, model results are compared to laboratory experiments. Laboratory experiments permit control over parameters such as material properties and bed geometries, which allow for easy comparison of flow theory with experiments.

The research conducted involved the development of granular flow experiments to demonstrate the strengths and limitations of the theoretical flow model Titan2D. In the first experiment, avalanches were initiated down a smooth inclined plane. The resulting flow propagation and deposition were compared to Titan2D simulations. The Titan2D model performs well in replicating the geometric propagation, position and timing of dry granular avalanches down smooth inclined beds.

In the second experiment, avalanches were initiated down a rough inclined plane. The rough plane was covered with an erodible bed and the resulting mobilization and deposition of static particles was measured and analyzed to better understand erosion rate over time. The data gathered from these experiments will be used to test the hypothesis that erosion can be incorporated into the Titan2D model by formulating criteria similar to Shield's stress criteria used in fluidized flow. The testing of this hypothesis is not included in this research.

In the last experiment, photoelastic discs were used in two-dimensional realizations of static non-cohesive granular systems. Measurements were taken of the resulting filamentary stress/force networks within the discs to gain a better understanding of the force distribution occurring within dynamic granular systems as

well as to validate the use of depth-averaging flow variables inherent in the Titan2D model. By analyzing the orientation of stress chains that developed in the photoelastic discs, it was observed that for the range of angles tested depth-averaging flow variables is a viable option.

Chapter 1

Introduction

The study of granular material has become more and more prevalent as the multitude of granular flow examples, both in industry and nature, become apparent. In nature, granular flows are found in numerous geomorphological processes including dune formation, delta clinoform and scoria cone growth and other avalanches of non-cohesive clasts, such as talus (Fig. 1.1).

Figure 1.1: Images of geomorphological processes in which granular flows are found. Clockwise from upper-left, scoria cone, talus, delta clinoform and dunes.

A particular granular flow phenomenon that could profit from immediate attention and exploration is volcanic flows, including debris avalanches and pyroclastic flows. There have been approximately 550 historical volcanic eruptions, the deadliest occurring in Tambora, Indonesia in 1815 killing 92,000 people (Blong, 1984). On May

1

18, 1980, after a series of explosions, a huge pyroclastic surge developed on Mount St. Helens. The intensity with which this lateral blast occurred was unexpected and resulted in a devastatingly large and unpredicted inundation area of 230 square miles (Lipman and Mullineaux, 1982). Virtually all of the deaths associated with volcanic eruptions are due to pyroclastic flows and lahars. One problem associated with the forecasting of volcanic flows is the difficulty in delineating what areas will be affected and to what extent (Iverson et al., 1998). The delineation of inundation area is directly dependent on the dynamics of granular flows in such cases where the particle concentration is sufficiently high that particle–particle interaction dominates momentum transfer. The present study focuses on an examination of these complex properties of granular materials and a comparison of results of granular flow experiments to numerical simulations.

1.1 Complexity of Granular Systems

Granular material behaves differently than any other type of material (Jaeger et al., 1996 A). Three factors that contribute greatly to the unusual and unique behavior exhibited by granular material are its ability to change its state, the dependence of unperturbed granular material movement upon two critical angles and the affect an erodible bed has on flow dynamics.

1.1.1 State of Granular Material

Depending on how granular material is prepared and excited, it can act like an unusual solid, liquid or gas. A sand pile below the angle of repose will behave like a solid, remaining at rest, while a sand pile above the angle of repose will begin to flow and behave like a liquid. This granular flow, however, is not typical of any fluid because movement is limited to a thin layer at the pile surface (Fig. 1.2). Like dense gas, granular material is made of discrete, non-cohesive particles. Unlike gases, the particles constituting granular material are relatively large and therefore thermal energy plays an insignificant role in its behavior. Lastly, the existence of static friction

between granular particles and the inelasticity of particle collisions differentiate granular material from gases by causing interactions to be dissipative which leads to a loss of homogeneity (Jaeger et al., 1996 A; Jaeger et al., 1996 B).
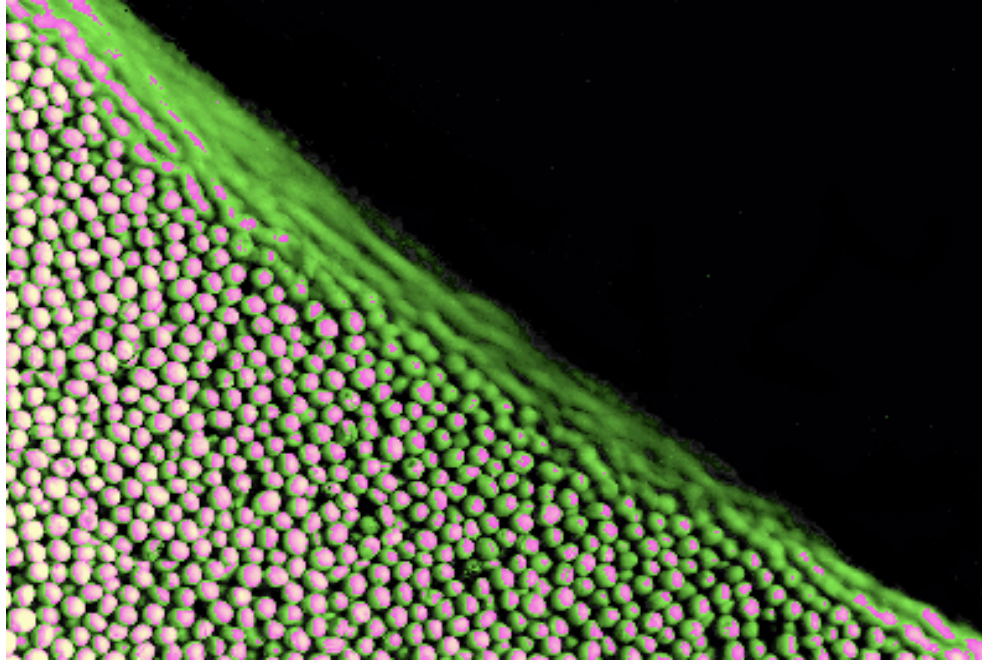
Figure 1.2: Image of a dry granular flow. The flow is limited to a thin layer at the pile surface (Jaeger et al., 1996 A).

1.1.2 Critical Angles

Static granular material on natural slopes is frequently near Coulomb yield failure bordering collapse where as flowing granular material generally loses energy quickly returning it to a static state (Behringer et al., 1999). Often precariously balanced between a static and dynamic state, granular material presents a challenging array of behaviors and characteristics governed by two critical angles.

The critical angles associated with dry granular material are the angle of repose and the maximum angle of stability (Fig 1.3). Material below the angle of repose will not avalanche while material above the maximum angle of stability will avalanche spontaneously and maintain motion until the surface slope has reached dynamic equilibrium at an angle less than the maximum angle of stability. Material existing at

an angle in between these two critical angles is in a metastable state and will flow only momentarily if perturbed (Daerr, 2001).
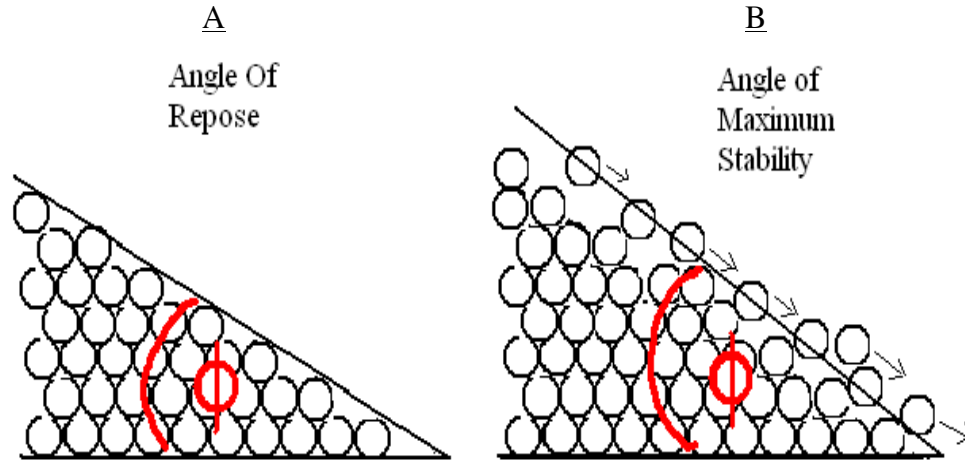
Figure 1.3: Image A depicts a pile of granular material resting at the angle of repose. Image B depicts a pile of granular material beginning to avalanche at the maximum angle of stability.

1.1.3 Erodible Beds

Particle-image velocimetry (PIV), used to evaluate the particle-velocity distributions in dry granular flows, suggests that a necessary criterion for unperturbed granular material at metastable angles to avalanche is the existence of an erodible bed (Tischer et al., 2001). When an avalanche occurs on an erodible bed, the mass of the solid particles constituting the flow can change by incorporating underlying eroded material as well as depositing material during the course of its propagation. Flow experiments carried out on erodible beds by Daerr (2001) show that the depth and degree to which an avalanche flowing down an erodible bed will mobilize bed particles generally relates to the relative height of the avalanche above the static layer. Tischer et al. (2001) determined that granular flows conducted on an erodible bed make a transition with downstream distance from a collisional, saltating flow to a frictional flow with shock wave characteristics. When this transition occurs, the avalanche front sets into motion static material and pushes it to the back of the flowing layer while depositing material on shallow slopes. This behavior restricts an avalanche front from

exceeding a maximum height by achieving a dynamic equilibrium between erosion and deposition (Daerr, 2001). The mobilization and deposition of particles within a flow adds new dimension to the complexity of dry granular flows that will be analyzed in this paper by conducting granular flow experiments on erodible beds.

1.2 Prior Work

Because of the complex and rich phenomenon of granular behavior, creating computational tools to simulate a granular volcanic flow and accurately predict the course it will take is difficult. Savage and Hutter (1989) introduced into the framework of dry granular avalanches models based on depth-averaged balance equations for mass and momentum, Mohr-Coulomb plastic yield criterion and a Coulomb dry friction law. For depth-averaged equations to adequately model the flows, Savage and Hutter assumed the flowing avalanche layer to be thin compared to its length. The theory is based on a simple Coulomb-type friction law for flow resistance. The friction law assumes that the ratio of shear stress at the bottom to normal stress is proportional over the depth of the granular flow, meaning the coefficient of friction is constant. Such models were able to describe the evolution and propagation of two-dimensional dry granular avalanches down a plywood surface at steep slopes (Savage & Hutter, 1989; Gray, Wieland & Hutter, 1999; Wieland, Gray & Hutter, 1999).

An extension of the Savage-Hutter depth-averaged model for granular avalanches was created for surfaces described in three-dimensions and was tested on curved beds (Greve, Koch & Hutter, 1994; Koch, Greve & Hutter, 1994; Hutter & Koch, 1991). The model was able to predict the evolution of height and depth-averaged downward and lateral velocity as functions of time and position. Using this model, satisfactory numerical predictions were made of the evolving geometry of a dry granular avalanche down an unconstrained inclined plane connected to a horizontal run-out plane by a transitional curve.

The onset of flow for granular material down rough surfaces is a result of complex behavior dependant upon both the inclination angle of the plane and the thickness of the granular layer (Pouliquen & Renaut, 1996; Daerr & Douady, 1999). Pouliquen & Forterre (2001) have shown that the Savage-Hutter simple solid friction law does not adequately describe this behavior. Pouliquen and Forterre developed a numerical model that describes dry granular avalanches down a rough inclined plane by modifying the Savage and Hutter depth-averaged model to incorporate a more realistic friction law. The relevant friction law is reliant upon the dependency of the stopping and starting angle of the flow upon the thickness of the layer. The model was able to quantitatively predict the spreading of a granular mass down a rough slope free of initial static particles from initiation to deposit (Pouliquen and Forterre, 2001).

Daerr (2001) studied the effects of triggering an avalanche in a metastable static layer on a rough inclined plane. Daerr analyzed the propagation velocities as well as the evolving shape of the avalanche front and was able to determine that the growth of an avalanche down an erodible bed reaches a dynamic equilibrium by reaching a constant speed regulated by avalanche height (Daerr, 2001).

As of yet not much work has been done towards developing models to simulate dry granular flows down rough surfaces with an erodible bed. Models of this nature need to be able to predict the geometry and propagation of the flow as well as how much of the underlying static material will be incorporated into the flow and how much flow material will be deposited during the course of its progression downwards. To develop a reasonable erosional model there needs to be a solid understanding of the particle interaction occurring between flow and static material as well as a working model for dry granular flow down smooth surfaces to use as a foundation.

1.3 Objectives and Purpose of Study

The research conducted involved the development of experiments to verify physical and computational models of dry granular avalanches down smooth and rough inclined planes. In the first set of experiments, avalanches were initiated on a smooth inclined plane. The resulting flow propagation and deposition were compared to simulations created with the Titan2D model being developed by the Geophysical Mass Flow Group, (GMFG) at SUNY, Buffalo. In the second set of experiments, avalanches were initiated on a rough inclined plane. The resulting mobilization and deposition of static particles was analyzed to gain a better understanding of the changes in erosion rate that occur with downstream distance. In the third set of experiments, photoelastic discs were used in two-dimensional realizations of static non-cohesive granular systems. Measurements were taken of the resulting filamentary stress/force networks within the discs to gain a better understanding of the force distribution occurring within granular systems.

The study of dry granular flow provides information necessary to developing a solid working debris flow theory. The granular flow experiments performed resulted in data that demonstrates the strengths and limitations of the theoretical model Titan2D.

I hypothesize:
1. Titan2D accurately models the flow of a granular avalanche on a smooth surface.
2. Erosion can be incorporated into the Titan2D model by formulating criteria similar to Shield's stress criteria used in fluidized flow.
3. The general vertical orientation of stress chains that develop in photoelastic discs used in 2D realizations of granular flow indicate that the depth-averaging of flow variables inherent in the Titan2D model is valid.

Chapter 2

Laboratory Granular Flows Down A Smooth Inclined Plane

2.1 Introduction

Developing numerical models to simulate natural phenomena requires a system of validation. It is not always convenient or possible to use actual events to validate models that simulate behaviors such as particle flow and interaction. Laboratory experiments permit control over parameters such as material properties and bed geometries, which allow for easy comparison of flow theory with experiments.

Savage and Hutter (1989) developed a granular flow model based on depth-averaged balance equations, Mohr-Coulomb plastic yield criterion and a Coulomb based friction law. They performed dry granular flow experiments down a glass-enclosed piece of plywood by releasing 2.54 cm size gravel from behind a gate. Because the roughness of the bed is not of the order of the flow particle size, the plywood platform is considered to be a smooth surface in these experiments. Comparison of experiment results to numerical output showed that the Savage and Hutter model was able to accurately describe the evolution and propagation of two-dimensional dry granular avalanches down a smooth plywood surface at steep slopes (Savage & Hutter, 1989; Gray, Wieland & Hutter, 1999; Wieland, Gray & Hutter, 1999).

An extension of the Savage-Hutter depth-averaged model was created for surfaces described in three-dimensions and tested on curved beds (Greve, Koch & Hutter, 1994; Koch, Greve & Hutter, 1994; Hutter & Koch, 1991). Greve et al. (1994) performed dry granular flow experiments down an unconstrained inclined plywood plane connected to a horizontal run-out plane by a curved cylindrical element. The plywood surface was varied with the application of three different bed linings: plexiglass, drawing paper and

no. 120 sandpaper. Because the roughness of the bed is not of the order of the flow
particle size each bed lining used in these experiments is considered to be a smooth
surface. A variety of granular materials, 3–5 mm in diameter, were released from either
a spherical cap or from behind a vertical plate and allowed to flow downstream until
they came to rest in the run-out zone. The model was able to predict the evolution of
height and depth-averaged downward and lateral velocity as functions of time and
position. Using this model satisfactory numerical predictions were made of the
evolving geometry of a dry granular avalanche down an unconstrained smooth curved
bed at steep slopes.

Numerical results for the Savage and Hutter model as well as the Greve, Koch and
Hutter model are limited to granular avalanches down smooth steep slopes. For this
study, granular flow experiments were conducted down smooth inclined planes at a
variety of different angles. The Titan2D simulations were then compared with the
laboratory experiments to validate that the model accurately simulates the dynamics of a
granular flow moving down a smooth surface at a variety of different angles.

2.2 General Characteristics of the Experiments

2.2.1 Experiment Set Up

Laboratory experiments were conducted using sand released onto a smooth
masonite plane. The plane measured 190 cm by 60 cm, and consisted of two parts. The
angle of inclination of the first section could be controlled precisely with an adjustable
mount. Sand particles were instantaneously released on this upper section from either a
small spherical cap or a large cylindrical container. The inclined upper section was
connected to the horizontal lower section, which was utilized as a run-out plane. The
particles released were playground sand grains sieved so that only the 2 ϕ (187-250 μm)
fraction was used. In each set of experiments the released material flowed down the
slope, spread and eventually came to rest in a tear shaped deposit. The propagation of

the mass was captured by videotape with a time-stamp while a grid of horizontal lines was projected onto the plane to aid in visualization (Fig. 2.1).
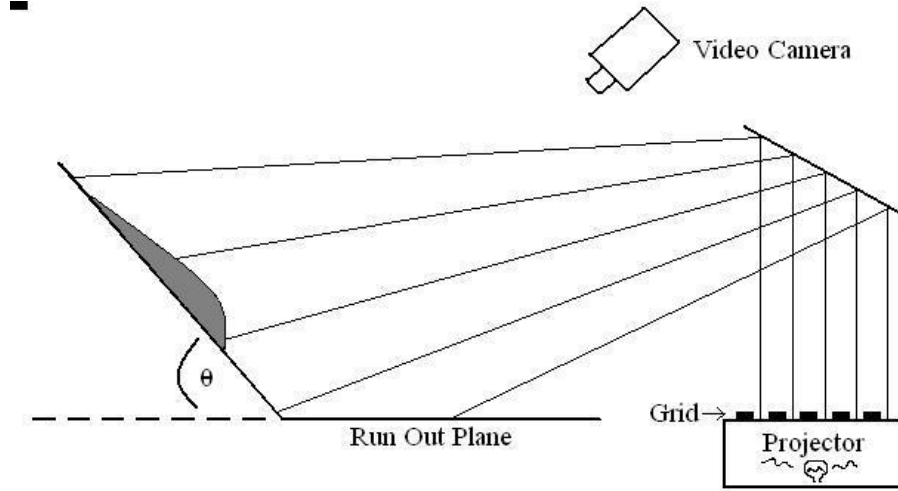
Figure 2.1: Schematic diagram of the experimental set-up.

The first experiments consisted of the instantaneous release of a fixed volume of sand from a spherical cap (radius = 2.5 cm). Three runs, each with a different release point (top, middle or bottom) were performed at a range of platform angles (Fig. 2.2). In order to control the amount of material released from the spherical cap, the mass of sand poured into the cap was weighed before each run (~ 43 g).
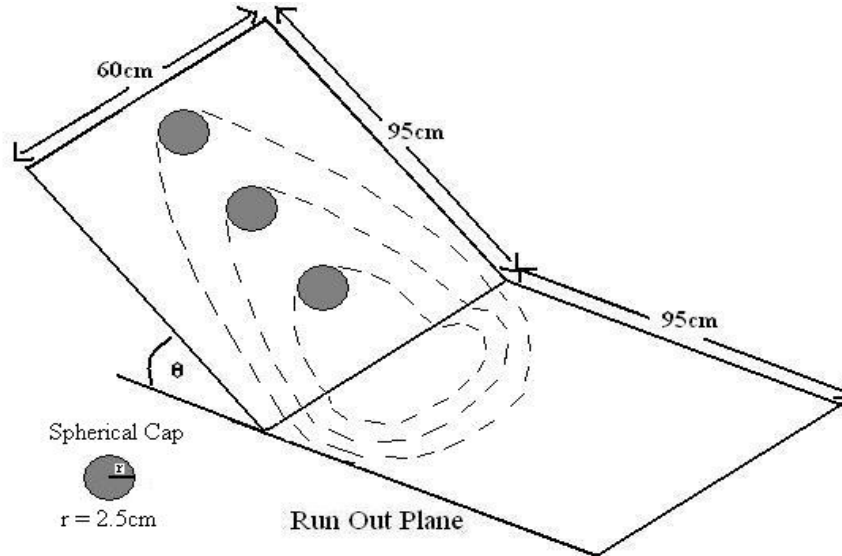
Figure 2.2: Schematic diagram of the release points used for the spherical cap experiments.

In a second set of experiments a fixed volume of sand was released from a glass cylinder (radius = 5.25 cm) positioned near the top of the inclined plane at a range of platform angles (Fig. 2.3). To control the amount of material released from the cylinder, the mass of sand poured into the cylinder was weighed before each run (~ 425 g). The 2 ϕ particles in this experiment were dyed blue for better visualization.
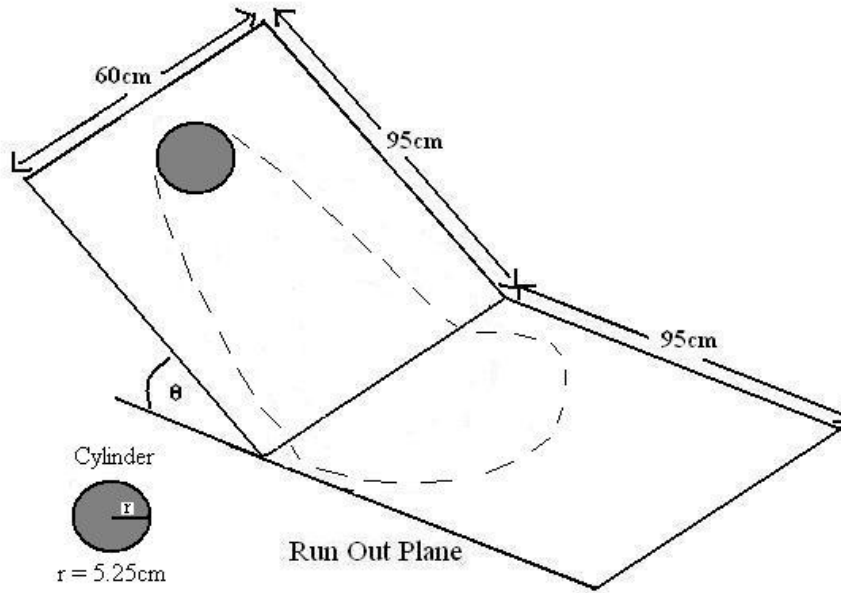
Figure 2.3: Schematic diagram of the release point used for the cylinder experiments.

Two important friction angles exist for granular material piled on a bed, the internal friction angle and the basal friction angle. The internal friction angle is a measure of the strength of the material's bulk and is attributable to two factors, the friction between individual grains and the geometrical interlocking between particles known as Reynolds dilatancy (Daerr, 2001). The basal friction angle is a measure of the friction between the grains and the bed surface. Experiments were conducted to measure both the internal and basal friction angles of 2 ϕ sand on a masonite bed surface.

Placing a small pile of sand on the masonite plane and then tilting the plane slowly until the pile began to move internally provided a measure of the internal friction angle. The angle at which visible internal movement occurred was measured and

11

recorded. The average internal friction angle achieved by performing this experiment was 37.3°.

The basal friction angle was measured in three different experiments. The first experiment consisted of placing a small amount of 2 φ sand on a masonite bed surface. The sand was smoothed out to a thin layer and a rectangular block of plastic was placed on top. The masonite plane was then slowly tilted until the block of plastic started to move. The angle at which this movement occurred was measured and recorded. The average basal friction angle achieved by performing this experiment was 18.2°. The second experiment to determine basal friction angle consisted of releasing 2 φ sand from a pipet onto an inclined masonite plane. The angle of the plane was then lowered until the sand released from the pipet no longer flowed down the plane. The angle at which movement ceased was measured and recorded. The average basal friction angle achieved by performing this experiment was 28.9°. The final basal friction angle experiment performed consisted of pouring 2 φ sand into a rectangular container. The top of the sand was smoothed out and then the container was then gently tilted onto its side causing the sand to avalanche and form an angle with the container. The angle at which the sand came to a rest after the container was tilted was measured and recorded. The average basal friction angle achieved by performing this experiment was 34.4°. An average of the data collected in the three experiments produced a mean basal friction angle of 27°.

2.2.2 Measurement Method

To measure precisely the geometry of the propagating granular flows as a function of position and time, a uniform centimeter scale was painted onto the edges of each plane. To aid in visualization of the scale every tenth centimeter marker was extended to be twice as long as the one-centimeter marks. A video camera was positioned as close to the plane as possible, its minimum distance and angle being dictated by the requirement that the entire flow zone from initiation to deposit be captured. The video camera provided a time-stamp on each frame telling the amount of time that had elapsed

since that camera was started. A horizontal grid was projected onto the plane to aid in visualization.

Once each experimental run reached completion the captured video frames, each representing 1/30 of a second, were retrieved with a digital frame grabber and saved as individual GIF images. Measurements of the propagating granular mass were taken directly from the frames by measuring the lateral spread at the top, middle and bottom of the mass, as well as the advance of the head and tail of the flow (Fig. 2.4). Due to geometrical distortions and time steps when the material of the flow was thinly spread, the edge of the flow was often difficult to ascertain. The error in the measurements of geometry and positions of the flow is estimated to range from 1.0-~ 2.5 cm. Geometry and position of the flow did not vary greatly between sequential frames therefore measurements were only taken from 5-10 selected frames per experiment.
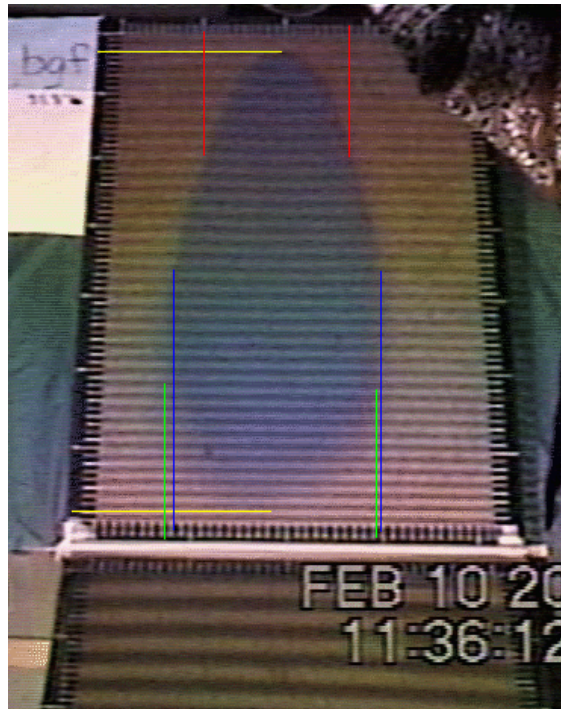
Figure 2.4: Image depicting how measurements were taken of the lateral spread (top = red lines, middle = blue lines, bottom = green lines) and the advance of the head and tail of the propagating flow (yellow lines).

2.3 Titan2D Numerical Model

TITAN2D is a numerical code designed to simulate dry granular avalanches over realistic representations of natural terrain. A Geographical Information System (GIS) interface provides the digital terrain, which is then combined with the numerical simulations.

The TITAN2D code is based on an incompressible Coulomb continuum model similar to models used to simulate a "shallow-water" granular flow (Denlinger and Iverson, 2001). The Mohr-Coulomb law on which the model is based imposes kinematic boundary conditions for stresses that occur in granular material at the free surface interface and at the basal surface interface. Like the Savage and Hutter (1989) model, the TITAN2D program uses depth-averaged conservation equations for mass and momentum. The conservation equations are solved with a Coulomb-type friction term that represents the interactions between the grain particles and the basal surface (Savage and Hutter, 1989). A parallel, adaptive mesh (Berger and Colella, 1989), Godunov scheme (Davis, 1988) is used to solve the resulting hyperbolic system of equations. Adaptive gridding and mesh refinement capabilities increase computational efficiency while enhanced computational power and decreased computing time is achieved by the Message Passing Interface (MPI) [http://www-unix.mcs.anl.gov/mpi/] Application Programmers Interface (API) ability to compute on multiple processors.

A Python scripted Graphical User Interface controls TITAN2D operations through user input parameters needed to successfully run the program. User input parameters include pile dimensions, starting coordinates, internal and basal friction angles and simulation time. Based on these parameters, the simulation is computed on a Digital Elevation Model (DEM) of the area of interest. The DEM is then formatted to operate in a GRASS (Geographic Resources Analysis Support System) GIS open source environment. GRASS GIS has many capabilities including raster, image processing, graphics production and topological vector functionality. Visual output from the simulation results are displayed through the TITAN2D viewer or other visualization

software packages. Output from the simulations include flow speed, run-up height, depth and inundation area. The higher the level of DEM quality and resolution the more accurate the rendered simulation will be (Patra et al., 2003; Pitman et al., 2003).

2.4 Data and Analysis

For the purpose of validating the Titan2D numerical model, data was collected on the lateral spread and advance of the head and tail of a dry granular flow from experiments performed by the release of sand from two different releasing mechanisms, a spherical cap and a cylinder. The data was then compared to simulation output generated using the same initial parameters as those used in the experiments. Experiments using the spherical cap as a release mechanism were run at three different angles of inclination, 37.4°, 40.1° and 43.6°. At each of these angles three runs were performed, each executed from a different release point. The first run was released near the top of the plane, the second in the middle and the third near the bottom. Experiments using the cylinder as a release mechanism were run at four different angles of inclination, 23.9°, 31.8°, 38.5° and 44.3°. Each run was executed from the same release point near the top of the inclined plane. The angles used in each experiment were chosen because they represent a range of angles that exist around the angle of repose and the angle of maximum stability.

Aside from the minor variations between the spherical cap and cylinder experiments, each experiment progressed similarly. A typical experiment proceeded as follows. The video was started and the operator placed the container flush to the inclined plane, the pre-weighed sand was then poured into the container. The container was then removed in a fluid motion, to avoid any unnecessary disturbance of the particles contained within. The mass of released particles then began to flow down the slope with the propagating head moving noticeably faster than the tail, which appeared to remain stationary for a short period of time. As the mass flowed down the slope, it spread laterally as well as downstream, causing the mass to rapidly evolve into a

teardrop shape. As the mass continued to move downstream, the teardrop shape elongated both laterally and downstream, while the tail eventually began to propagate downstream. Once the flowing mass reached the lower run-out section the head began to deposit in a teardrop shape that was less elongated in the downstream direction than the actively propagating mass. The position of the final deposit was dependant upon several variables including the mass of particles released, the release point and the angle of inclination. In the spherical cap experiments, the final deposit came to rest in a teardrop shape entirely on the lower run-out plane. The exception to this scenario was when the mass was released near the bottom of the inclined plane at a low angle of inclination. When these two factors existed, the final deposit came to rest in a conic shape with its base on the run-out plane and apex located at some height on the inclined plane that was dependent upon the angle of inclination. In the cylinder experiments, the final deposit most often came to rest in a conic shape with its base located on the run-out plane and its apex located at some height on the upper inclined plane. The exception to this scenario occurred when the angle of inclination was very high in which case the final deposit came to rest in a teardrop shape entirely on the lower run-out plane. Regardless of the mass of particles released, experiments performed at angles within the range of the basal friction angle resulted in the entire mass coming to rest in a teardrop shape on the upper inclined plane.

The main method of analysis is a quantitative comparison of mid-flow lateral spread and distance between the head and tail measurements for Titan2D simulated and observed avalanches, although a qualitative comparison proves valuable as well (Fig. 2.5). Comparison of the simulated and observed flow's lateral spread and head and tail advance involves the following steps: selected images captured of each experiment run were analyzed and measurements were made of the observed lateral spread at the top, middle and bottom of the mass, as well as the advance of the head and tail of the flow as discussed in section 2.2.2.

Numerical simulations were run using the same values for angle of inclination, initial pile dimensions and release point as those used in the experiments. Based on the

16

internal and basal friction angle tests discussed in section 2.2.1, the internal friction angle was chosen to be 37.3° and the basal friction angle was chosen to be 27°. Along with
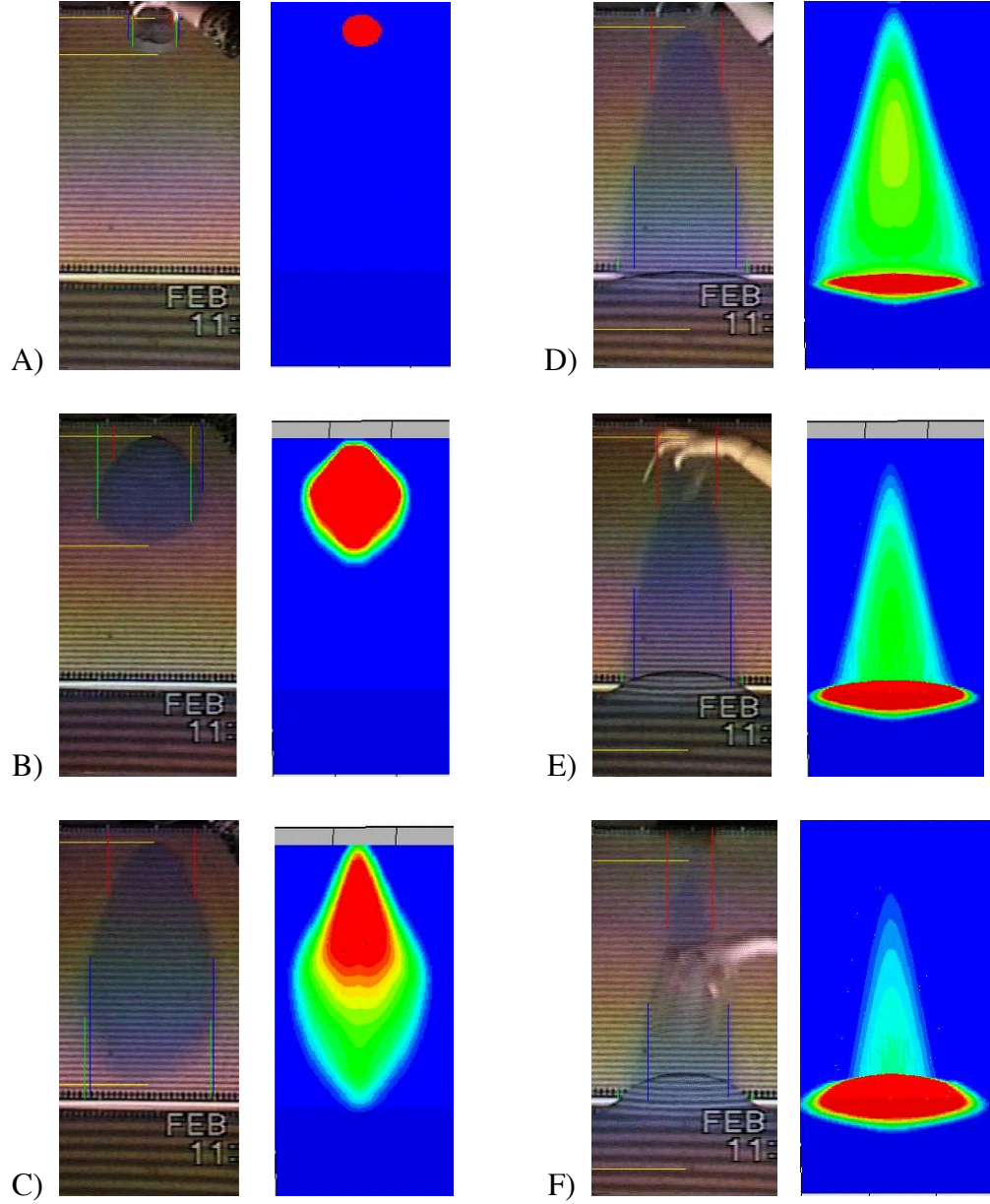
Figure 2.5: Visual comparison of experiment images (left image in groups A-F) to numerical images (right image in groups A-F) showing the evolution of a granular flow from initiation A, to deposition F. The colored contours in the numerical images each represent different flow thicknesses. Warm tones are thicker than cool tones.

visual output, the Titan2D program also generated data on the lateral spread and distance between the head and tail of a flow for three defining edge contours for each

time-step. The numerical contours represent the edge of the flow defined by different flow thicknesses, 0.001 mm, 0.0005 mm and 0.00025 mm and were chosen because they best encompass the experimental data points. The 0.001 mm contour represents a defining edge of 4-5 grain diameters thick, the 0.0005 mm contour represents a defining edge of 2-3 grain diameters thick and 0.00025 mm represents a defining edge of one-grain diameter thick.

The lateral spread and distance between the tail and head of the flow at different times during the course of each flow were graphed for both the observed and simulated runs. The graphs provide information on any general trends in the positions and geometry of simulated vs. observed granular mass flow down smooth inclined planes.

2.5 Results and Discussion

The Titan2D model equations and numerical solver were tested against results from experiments. What follows are the results from a comparison of known data with numerical realizations for avalanches initiated down a smooth inclined plane at a variety of angles. We investigate the lateral spread, advance of the head and tail and the general position and timing of flows at a series of time steps.

2.5.1 Spherical Cap Experiments: Lateral Spread

Data on the lateral spread of a flow was collected from experiments and simulations initiated at three different angles of inclination. The data was then graphed to reveal any general trends between experimental results and numerical output.

The graphs seen in Figures 2.6, 2.7 and 2.8 show similar overall characteristics between experimental and numerical flows as well as good quantitative comparison of the evolving pile shape. In all scenarios, the general trend exhibited is for numerical output generated by contour 0.0005 mm to match up well with the experimental data. There are two exceptions to this general trend, the first of which is exhibited in Figure

18

2.6 Graph C. In this graph, numerical output generated by contour 0.001 mm best matches experimental data. The particles in this run were released from such a low release point that the avalanche did not pick up significant speed on its way down the inclined plane. With negligible speed and distance to travel, the particles were not able to spread much in the lateral direction. With nominal lateral spread, the defining edge of the flow remained deep, which is why the data generated by the deepest contour, 0.001 mm, match up best with the experimental data. The second exception to the general trend is exhibited in Figures 2.6, 2.7 Graph A and Figure 2.8 Graph A and B. In these graphs, the trend is for the numerical output generated by contour 0.0005 mm to initially match up with the experimental data. However, at the end of the run experimental data shows a noticeable increase in value that the numerical output does not demonstrate. This behavior occurs in the observed flows as the propagating mass makes the transition from flowing down the inclined plane to depositing on the run-out plane. The experiments that exhibit this behavior share either a release point at the top of the plane (Figures 2.6, 2.7 and 2.8 Graph A) or a high angle of inclination (Figure 2.8 Graph B). These variables contribute to an increase in the propagating flows overall velocity and mass. In the experiments, as the avalanche deposits on the run-out plane, a small pile forms at the head of the flow. As more particles reach the plane, they splash down into the small pile of particles causing it to spread out in a ballistic manner both laterally and in the downstream direction. The Titan2D simulations do not model this behavior.

Figure 2.6: Graph of the lateral spread of a flow at different time steps, for observed and simulated avalanches initiated at an angle of 37.4°. Gaps in numerical data represent an unreasonably low output of −1.0 E+30.
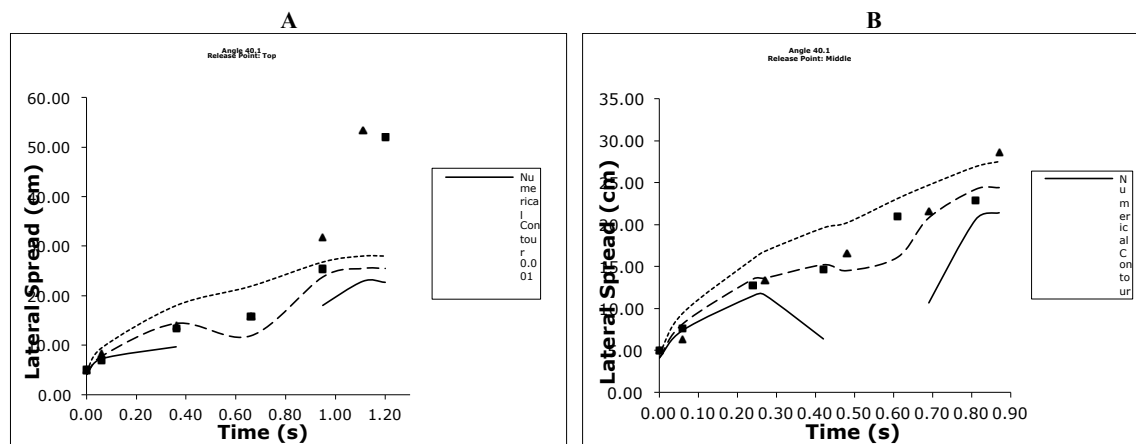
Figure 2.7: Graph of the lateral spread of a flow at different time steps, for observed and simulated avalanches initiated at an angle of 40.1°. Gaps in numerical data represent an unreasonably low output of −1.0 E+30.
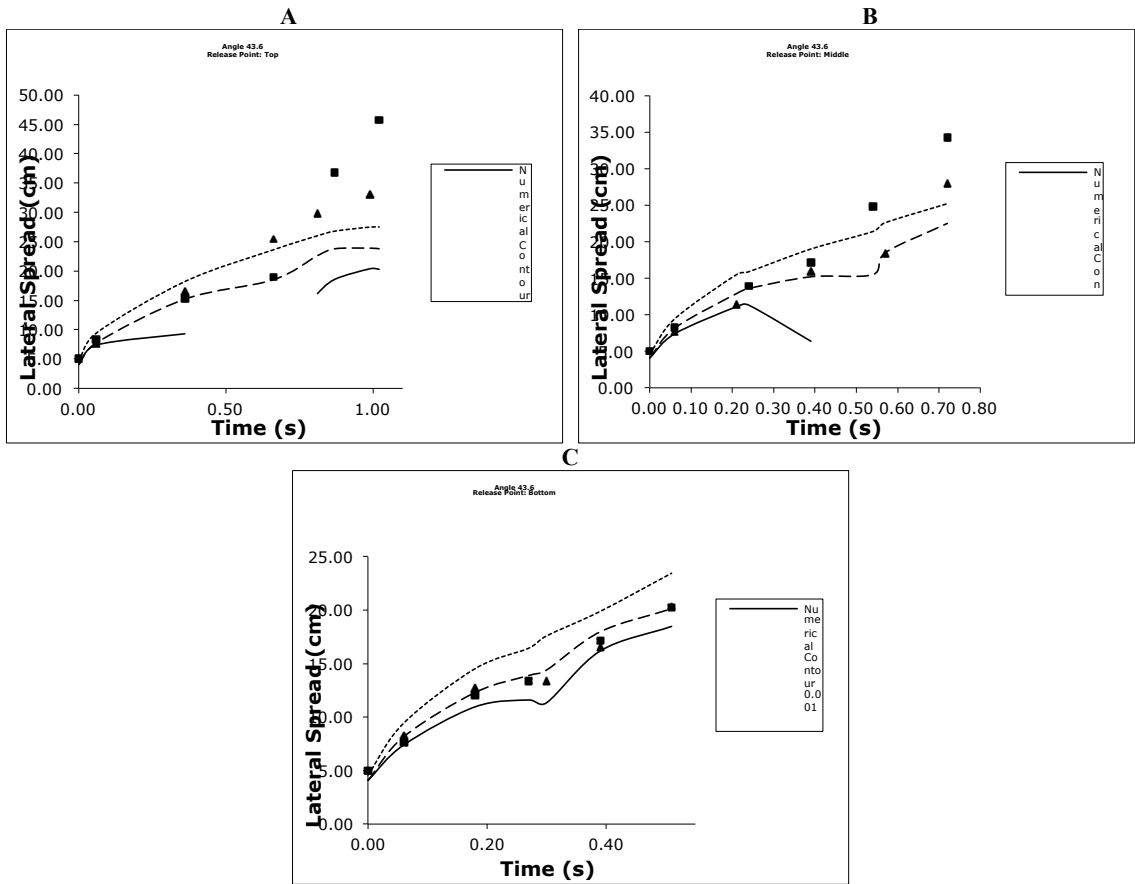
Figure 2.8: Graph of the lateral spread of a flow at different time steps, for observed and simulated avalanches initiated at an angle of 43.6°. Gaps in numerical data represent an unreasonably low output of –1.0 E+30.

2.5.2 Spherical Cap Experiments: Distance Between The Head And Tail

Data on the distance between the head and tail of a flow was collected from experiments and simulations initiated at three different angles of inclination. The data was then graphed to reveal any general trends between experimental results and numerical output.

The graphs seen in Figures 2.9, 2.10 and 2.11 show similar overall characteristics between experimental and numerical flows as well as good quantitative comparison of the evolving pile shape. However, experimental and numerical flows initiated from release points near the top or middle of the plane do not show good overall quantitative

21

comparison in evolving distance values between the head and tail of a flow (Figs. 2.9, 2.10 and 2.11 Graphs A and B). For avalanches initiated from these release points numerical output generated by contour 0.00025 mm initially matches up well with experimental data but after ~ 0.4 seconds numerical data deviates from experimental data revealing much smaller values. This behavior occurs in the experiments directly before the propagating mass reaches the run-out plane. The largest variation between numerical and experimental values, for avalanches initiated near the top or middle of the inclined plane, occurs at the end of the flow. At this point, the numerical output is significantly lower in value then the experimental data. This behavior occurs in the observed flows at the end of the flow when the propagating mass is depositing on the run-out plane. It is possible that by using a numerical contour representative of a thinner defining edge than any of the contours currently in use, output could be generated that would better correspond to experimental data recorded during the time period when numerical data initially deviates from experimental data up until immediately before the end of the flow. The large variation in numerical and experimental values displayed at the end of the run is not a behavior a thinner contour would be able to compensate for. The increased distance exhibited in experimental data at the end of each run occurs as a result of the following behavior. As the avalanche deposits on the run-out plane, a small pile forms at the head of the flow. As more particles reach the plane, they splash down into the small pile of particles causing it to spread out in a ballistic manner both laterally and in the downstream direction. The Titan2D simulations do not model this behavior.

Despite the significant deviation of experimental values from numerical values for avalanches initiated near the top or middle of the plane, as the release point moves downstream, variation between experimental and numerical values decreases. Once the release point reaches the bottom of the inclined plane, numerical output generated by contour 0.0005 mm begins to match up well with experimental data both in pile shape and value (Fig. 2.9 and 2.11, Graph C).

22

A

B

Angle 37.4
Release Point: Top

Angle 37.4
Release Point: Middle

C

Angle 37.4
Release Point: Bottom
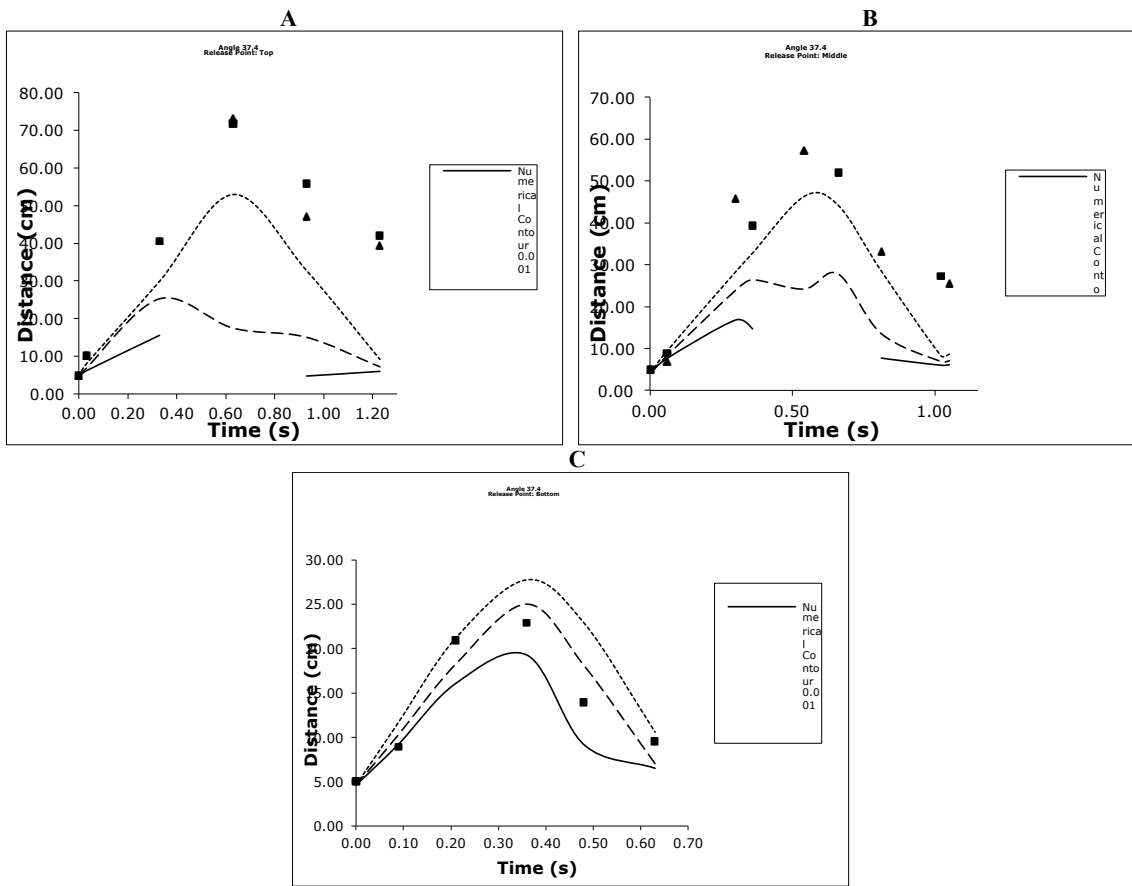
Figure 2.9: Graph of the distance between the head and tail of a flow at different time steps, for observed and simulated avalanches initiated at an angle of 37.4°. Gaps in numerical data represent an unreasonably low output of –1.0 E+30.

A

B

Angle 40.1
Release Point: Top

Angle 40.1
Release Point: Middle
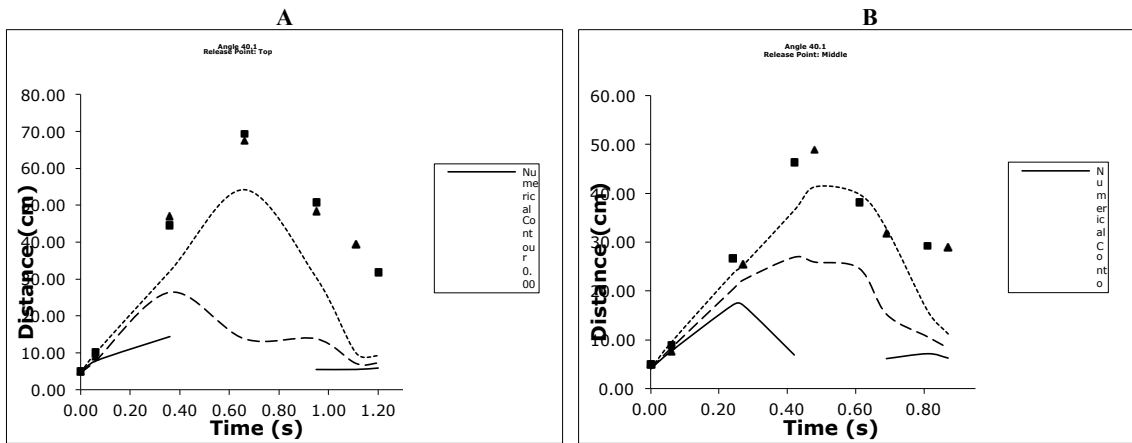
Figure 2.10: Graph of the distance between the head and tail of a flow at different time steps, for observed and simulated avalanches initiated at an angle of 40.1°. Gaps in numerical data represent an unreasonably low output of –1.0 E+30.
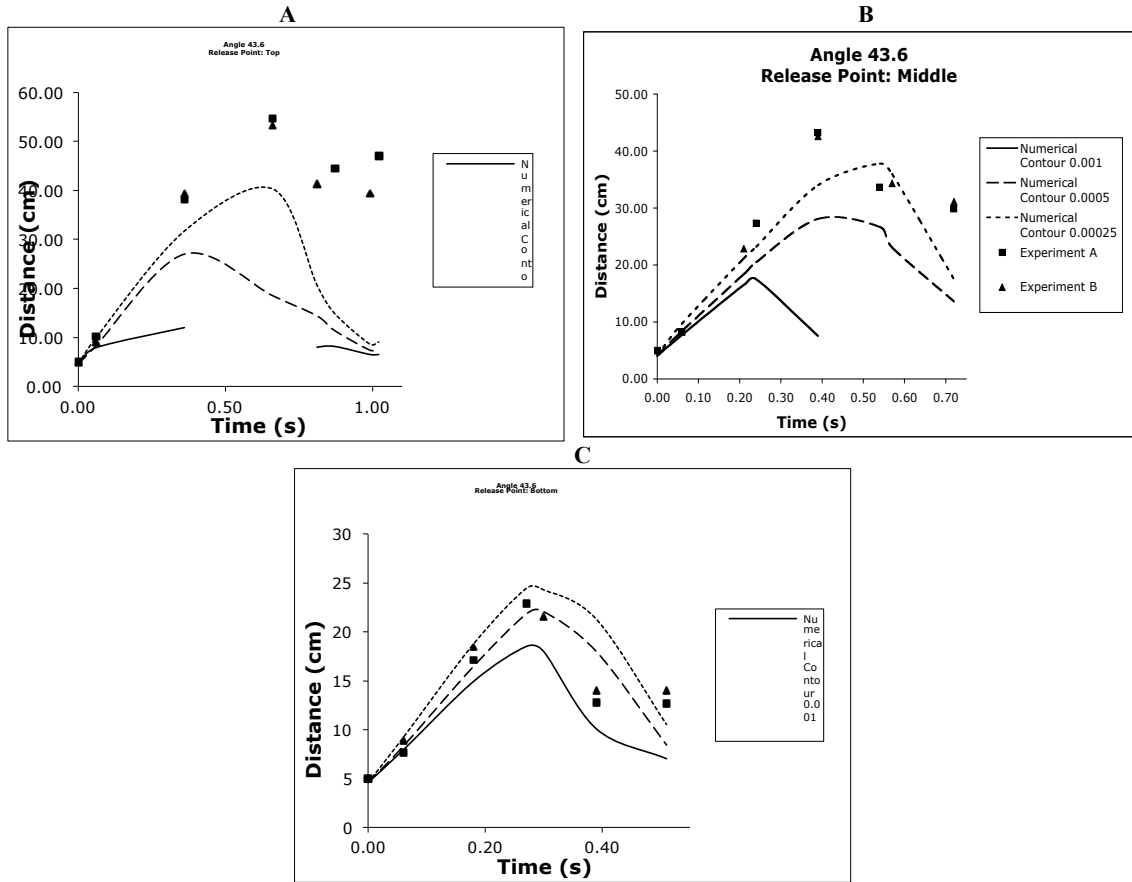
Figure 2.11: Graph of the distance between the head and tail of a flow at different time steps, for observed and simulated avalanches initiated at an angle of 43.6°. Gaps in numerical data represent an unreasonably low output of –1.0 E+30.

2.5.3 Cylinder Experiments: Lateral Spread

Data on the lateral spread of a flow was collected from experiments and simulations initiated at four different angles of inclination. The data was then graphed to reveal any general trends between experimental results and numerical output.

The graph seen in Figure 2.12 shows overall similar characteristics between experimental and numerical flows as well as good quantitative comparison of the evolving pile shape. However, experimental and numerical flows do not show good

overall quantitative comparison in evolving lateral spread values. In Figure 2.12, numerical output generated by contour 0.001 mm matches up well with experimental data in pile shape but not in value. Numerical data reveals much larger values for lateral spread than experimental data. For this experiment, the angle of inclination is within the range of the basal friction angle and resulted in the entire mass coming to rest in a teardrop shape on the upper inclined plane. The particles in this run were released at such a low angle of inclination that the avalanche did not pick up significant speed on its way down the inclined plane. With negligible speed, the particles did not spread in the lateral direction. With minimal lateral spread, the defining edge of the flow remained deep. It is possible that by using a numerical contour representative of a deeper defining edge than any of the contours currently in use, output could be generated that would better correspond to experimental data recorded for angle 23.9°.
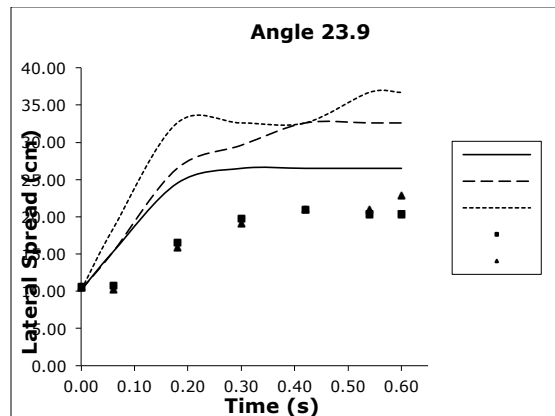
Figure 2.12: Graph of the lateral spread of a flow at different time steps, for observed and simulated avalanches initiated at an angle of 23.9.

Graphs A and B (Fig. 2.13) show similar overall characteristics between experimental and numerical flows at the beginning of the flow. However, mid-way through, the experimental and numerical flows cease to show similarity in pile shape or evolving lateral spread values. Graph C (Fig. 2.13) shows similar overall characteristics between experimental and numerical flows as well as good quantitative comparison of the evolving pile shape. However, the experimental and numerical flows do not show good overall quantitative comparison in evolving lateral spread values. In Figure 2.13 Graphs A, B and C, numerical output generated by contour 0.001 mm initially matches

up well with experimental data, but after ~ 0.55 seconds numerical output deviates from experimental data both in shape and value. As the numerical output increases in value eventually reaches a plateau, experimental data in graphs A and B decrease in value while experimental data in graph C plateaus. At the end of each run, experimental data show a noticeable increase in value that the numerical output does not demonstrate. This behavior occurs in the experiments as the propagating mass makes the transition from flowing down the inclined plane to depositing on the run-out plane. It is possible that by using a numerical contour representative of a deeper defining edge than any of the contours currently in use, output could be generated that would better correspond to experimental data recorded during the time period when numerical data initially deviates from experimental data up until immediately before the end of the flow. However, the significant increase in experimental values displayed at the end of the run is not a behavior for which a deeper contour would compensate. The increase in values exhibited in experimental data at the end of each run occurs as a result of the following behavior. As the avalanche deposits on the run-out plane, a small pile forms at the head of the flow. As more particles reach the plane, they splash down into the small pile of particles causing it to spread out in a ballistic manner both laterally and in the downstream direction. The Titan2D simulations do not model this behavior.
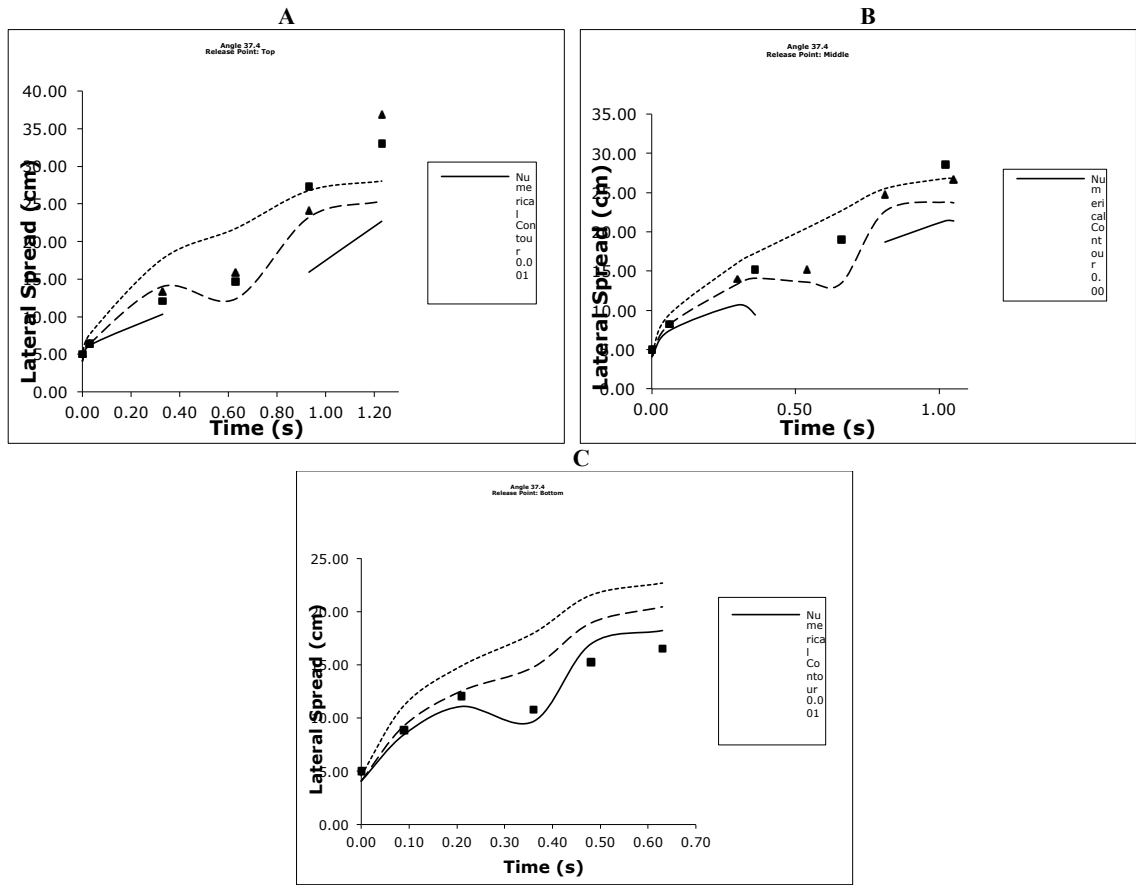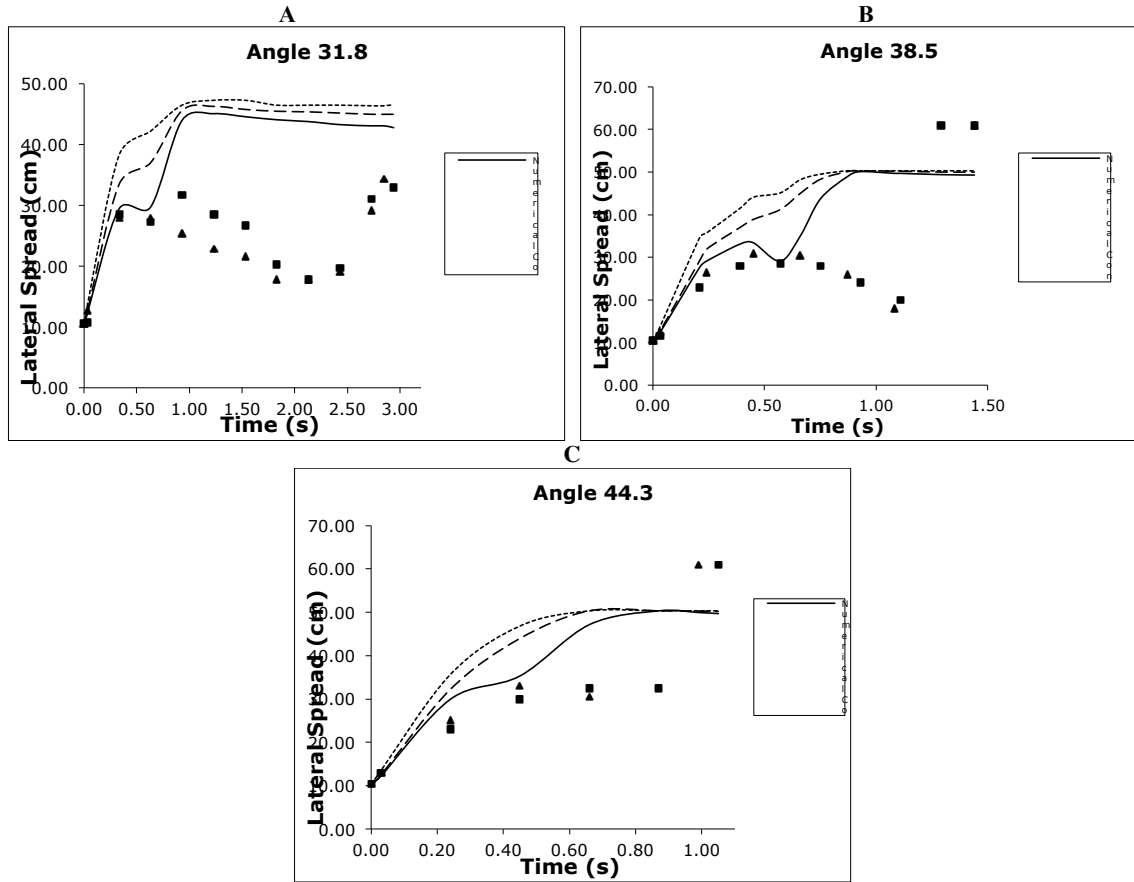
Figure 2.13: Graph of the lateral spread of a flow at different time steps, for observed and simulated avalanches initiated at angles of 31.8°, 38.5° and 44.3°.

2.5.4 Cylinder Experiments: Distance Between The Head and Tail

Data on the distance between the head and tail of a flow was collected from experiments and simulations initiated at four different angles of inclination. The data was then graphed to reveal any general trends between experimental results and numerical output.

The graph seen in Figure 2.14 shows similar overall characteristics between experimental and numerical flows at the beginning of the flow. However, mid-way

through, the experimental and numerical flows cease to show similarity in pile shape, evolving lateral spread values and timing. Initially, numerical output generated by contour 0.00025 mm matches up well in pile shape and value with experimental data, but after ~ 0.35 seconds numerical output deviates from experimental data revealing a plateau in values while experimental data continues to increase in value. This shows that the avalanche simulated by Titan2D at angle 23.9° underestimates the distance between the head and tail of the final deposit as well as the amount of time it would take for the run to come to completion. It is possible that by using a numerical contour representative of a thinner defining edge than any of the contours currently in use, output could be generated that would better correspond in value and time to experiment data recorded for this angle.
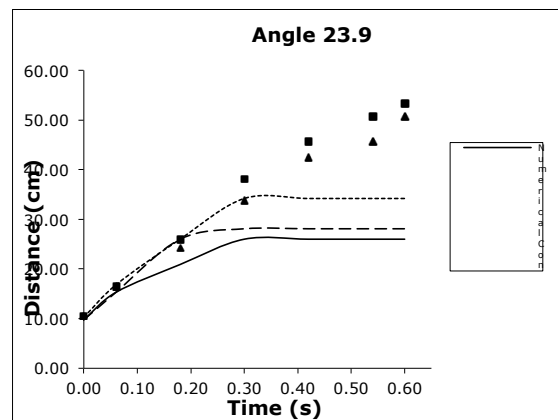
Figure 2.14: Graph of the distance between the head and tail of a flow at different time steps, for observed and simulated avalanches initiated at an angle of 23.9.

The graphs seen in Figure 2.15 show similar characteristics between experimental and numerical flows as well as good quantitative comparison of the evolving pile shape. However, experimental and numerical flows do not show good overall quantitative comparison in evolving distance values between the head and tail of a flow. Numerical output generated by contour 0.0005 mm initially matches up well in value with experimental data but, after ~ 0.6 seconds numerical output deviates from experimental data revealing much smaller values. In graph A, numerical data peaks almost a full second before the experimental data and indicates with a plateau in values that the avalanche run is finished almost a second and a half before the observed avalanche

ends. This indicates that the Titan2D simulated avalanche underestimates not only the greatest distance achieved between head and tail, but the time it takes for an avalanche initiated at an angle of 31.8° to reach final deposition. In graph B, numerical output peaks only 0.15 seconds before experimental data. It is possible that by using a numerical contour representative of a thinner defining edge than any of the contours currently in use, output could be generated that would better correspond to experimental data recorded for angle 38.5° during this time period. However, numerical output indicates, with a plateau in values, that the avalanche run is finished ~ 1/3 of a second before the observed avalanche ends. Although the difference in timing is not as significant as that found for angle 31.8°, this does indicate that the Titan2D simulated avalanche underestimates the time it takes for an avalanche initiated at an angle of 38.5° to reach its final deposit. In graph C, despite some variation in values after numerical and experimental data peak, numerical data peaks only 0.1 second before experimental data and ends at relatively the same time as the experimental data. It is possible that by using a numerical contour representative of a thinner defining edge than any of the contours currently in use, output could be generated that would better correspond to experimental data recorded for angle 44.3°.
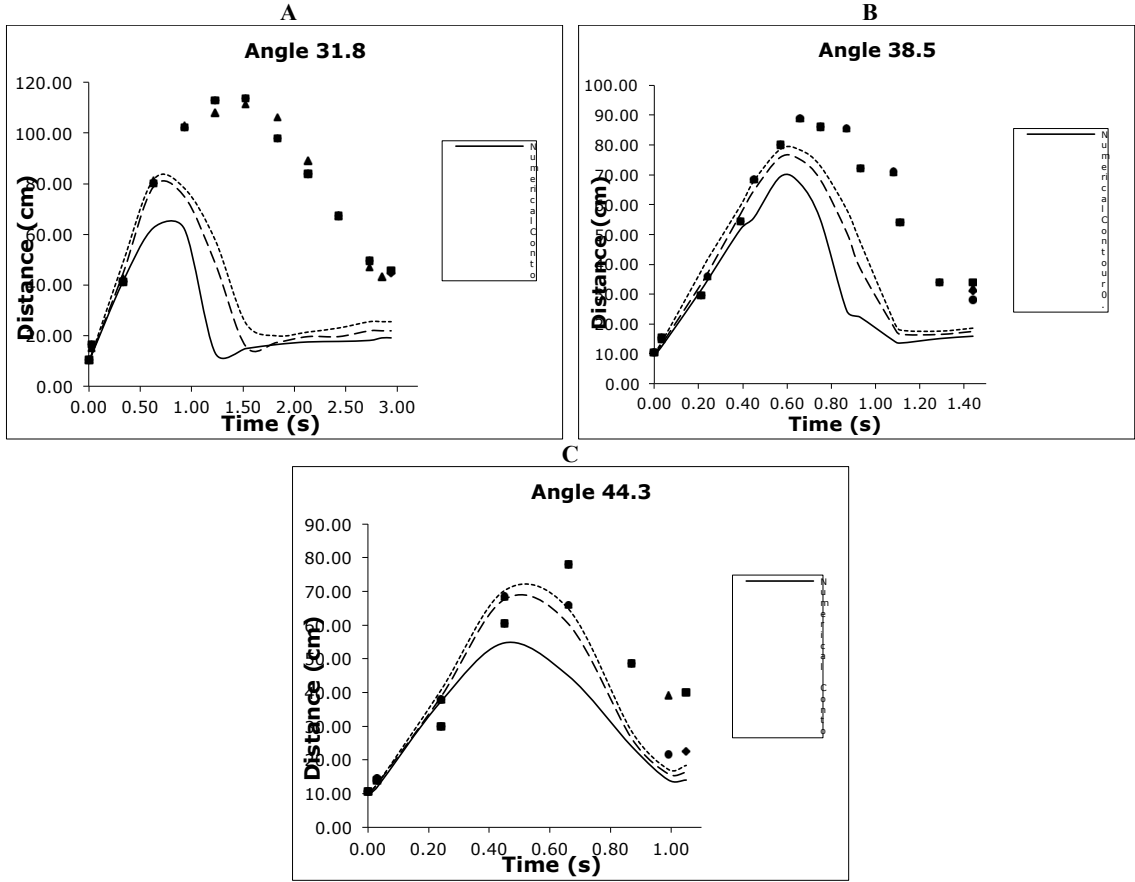
Figure 2.15: Graph of the distance between the head and tail of a flow at different time steps, for observed and simulated avalanches initiated at angles of 31.8°, 38.5° and 44.3°. Measurements made directly of the final deposit show larger values for the distance between the head and tail then measurements made from computer images of the flow. Experiment's representing a measurement taken directly from the final deposit are labeled maximum while experiments representing a measurement made from computer images of the final deposit are labeled minimum.

2.6 Conclusions

The present research is a quantitative comparison of experimental and numerical results recorded on the evolution of dry granular avalanches initiated down a smooth

inclined plane at a variety of angles. Despite some discrepancies, the results suggest that the Titan2D model provides adequate fidelity to several characteristics of real, small-scale physical flows including pile shape, position and dimensions. In comparing experimental and numerical results, perhaps the most common reason for discrepancies occurred because of the low gradient of the pile height near the flow edge. By incorporating a larger range of numerically defined contours many of the inconsistencies between numerical and experimental values would be eliminated. In general, the overall positive correlation between experimental and numerical results validates the use of such a tool for the simulation of geophysical mass flows.

Chapter 3

Laboratory Granular Flows Down A Rough Inclined Plane With An Erodible Bed

3.1 Introduction

Developing numerical models to simulate natural phenomena requires a system of validation. It is not always convenient or possible to use actual events to validate models that simulate behaviors such as particle flow and interaction. Laboratory experiments permit control over parameters such as material properties and bed geometries, which allow for easy comparison of flow theory with experiments.

Dry granular flows over rough terrain with an erodible bed increase in volume downstream as sediment is eroded. The volume of sediment a flow of this type consists of is strongly related to the intensity of hazard it may incur (Papa et al., 2003). This relationship makes the study or erosion rate essential in debris flow analysis.

The onset of flow for granular material down a rough surface is a result of complex behavior dependant upon both the inclination angle of the plane and the thickness of the granular layer (Pouliquen & Renaut, 1996; Daerr & Douady, 1999). This behavior has proven to be insufficiently described by the Savage-Hutter simple Coulomb based friction law. Pouliquen and Forterre (2001) developed a numerical model that describes dry granular avalanches down a rough inclined plane by modifying the Savage and Hutter depth-averaged model to incorporate a more realistic friction law. The relevant friction law is reliant on the dependency of the stopping and starting angle of the flow upon the thickness of the layer. Pouliquen and Forterre performed dry granular flow experiments down a rough inclined plane both with and without an initial static layer present. The plane was made rough by gluing a layer of 500 μm glass beads to its surface. Spherical caps filled with 500 μm glass bead particles were released at the top of the inclined plane and flowed down either a rough surface free of static

particles or a rough surface with an erodible bed of 500 μm glass beads. The model was able to satisfactorily predict the spreading of a granular mass when flow was released on a rough plane free of particles but failed to predict the spreading of a granular mass when the flow was released on a rough plane with an initial static layer (Pouliquen & Forterre, 2001).

Daerr (2001) performed granular flow experiments down an inclined plane at a metastable angle with an initial static layer. The inclined plane was covered with a velvet cloth so that the glass beads (180-300 μm) would have greater friction with it than each other. The glass beads were released from the top of the inclined plane leaving a static layer of beads behind that formed the deformable bed. The static layer was then perturbed initiating an avalanche. Daerr was able to determine that despite the increasing volume of the avalanching mass, the growth of an avalanche down an erodible bed achieves a dynamic equilibrium by reaching a constant speed regulated by avalanche height (Daerr, 2001). Daerr did not compare his experimental results to a model nor did he expand his research to include analysis of erosion of the static layer over time.

Neither Pouliquen and Forterre nor Daerr extended their work to describe the rate at which an avalanche erodes deformable material with downstream distance or was successful at developing a numerical model that incorporates erosion. For this paper granular flow experiments were conducted down a rough inclined plane at a variety of angles. The rough plane was covered with an erodible bed and the resulting mobilization and deposition of static particles was measured and analyzed to better understand erosion rate over time. This data was gathered to test the hypothesis that erosion can be incorporated into the Titan2D model by formulating criteria similar to Shield's stress criteria used in fluidized flow. The Shield's criterion essentially stipulates that once a flow exceeds a threshold shear stress, erosion will occur. Below this threshold, no erosion will occur. The threshold shear stress is a function of slope angle.

3.2 General Characteristics of the Experiment

3.2.1 Experiment Set Up

Laboratory experiments were conducted using sand released onto a rough masonite plane with an initial static layer. A sedimentation container was positioned at the base of the plane to capture any particles that flowed off of the inclined plane. The plane measured 95 cm by 60 cm and was made rough by gluing 36 grit (480 μm) sandpaper to the surface. The angle of inclination of the plane could be controlled precisely with an adjustable mount. An erodible bed was created on the roughed plane by broadcasting a stable layer of sand particles onto the plane. The thickness of the erodible bed was determined by the height of the broadcast layer when the particles stopped moving down the plane. This height was no more than a fraction of a centimeter deep. The particles remained stable at experimental test angles because the friction angle between the sand and the sandpaper was much greater than the angle of inclination of the slope. The particles used to create the erodible bed were playground sand grains sieved so that only the 2.5 ϕ (125-187 μm) fraction was used. The propagation of the mass was captured by videotape with a time-stamp while a grid of horizontal lines was projected onto the plane to aid in visualization (Fig. 3.1).
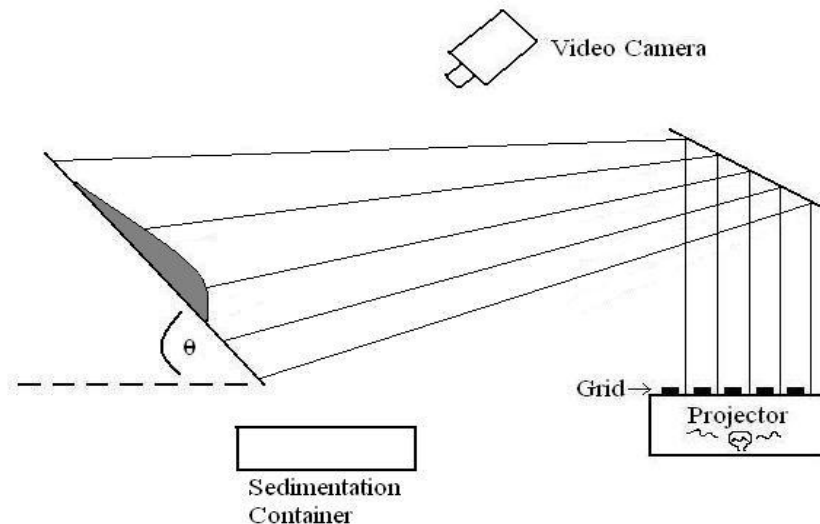
Figure 3.1: Schematic diagram of the experiment set-up.

34

Four runs, each with a different release point (top, top-middle, bottom-middle or bottom) were performed at four angles of inclination. Duplicate experiments were performed for each angle of inclination. A fixed volume of sand was instantaneously released at one of the four release points onto the erodible bed from a large cylindrical glass container (radius = 5.25 cm). The particles then flowed down the inclined plane over the erodible bed into a sedimentation container positioned below the base of the plane (Fig. 3.2). The particles released were playground sand grains sieved so that only the 2 φ (187-250 μm) fraction was used. The 2 φ particles were dyed blue for better visualization. Different release points were used to derive an erosion gradient between each successive release point based upon the mass of erodible material in the catch basin at the end of each run. The erosion gradient and flow speed data was then used to estimate erosion rate. To control the amount of material released from the cylinder, the mass of sand poured into the cylinder was weighed before each run (~ 425 g).
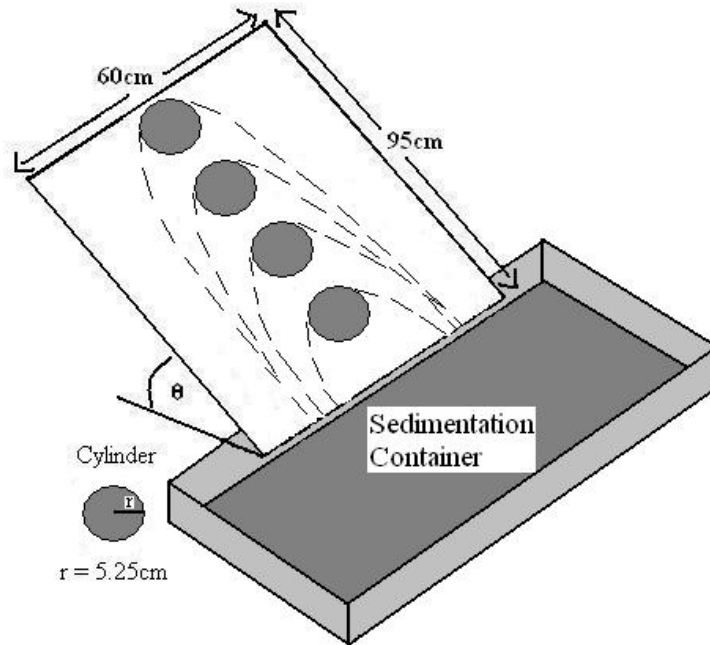
Figure 3.2: Schematic diagram of the release points used in the rough inclined plane experiments.

The released material flowed down the slope over the erodible bed, spreading both laterally and in the downstream direction. As the mass propagated in the downstream

direction, particles from the erodible bed were entrained at the front then pushed to the back where many were released from the flowing mass and deposited back onto the inclined plane. With time, some of the 2 ϕ particles ceased movement creating a tear shaped deposit on the inclined plane while the rest of the entrained 2-2.5 ϕ avalanche particles continued to flow off the plane into the sedimentation container positioned below.

Two important friction angles exist for granular material piled on a bed, the internal friction angle and the basal friction angle. Experiments were conducted to measure both the internal and basal friction angles of 2 ϕ sand on a masonite bed surface. Methodology and results of the friction angle experiments can be found in section 2.2.1.

3.2.2 Measurement Method

To precisely measure the geometry of the propagating granular flows as a function of position and time, a uniform centimeter scale was painted onto the edges of each plane. To aid in visualization of the scale, every tenth centimeter marker was extended to be twice as long as the one-centimeter marks. A video camera was positioned as close to the plane as possible, its minimum distance and angle dictated by the requirement that the entire flow zone from initiation to spilling over the bottom edge of the inclined plane be captured. A sedimentation container was placed beneath the bottom edge of the inclined plane to capture all of the particles that spilled over the end of the inclined plane. The video camera provided a time-stamp on each frame telling the amount of time that had elapsed since that camera was started. A horizontal grid was projected onto the plane to aid in visualization.

Once each experimental run ended, the sand captured in the sedimentation container was sieved into two masses representing 2 and 2.5 ϕ fractions. Each fraction was then weighed. The mass of 2 ϕ sand located in the sedimentation container, was subtracted from the mass initially released to determine how much of the original

avalanching mass reached the sedimentation container and how much was deposited on the inclined plane. The mass of 2.5 ϕ sand located in the sedimentation container provided a measurement of the amount of material eroded from the deformable bed that remained entrained in the avalanche. The mass of eroded 2.5 ϕ sand recorded for each release point for an angle, was then used in the erosion rate equation explained below to determine the rate of erosion occurring between sequential release points. Erosion rate was determined for a flow in three sections (Fig. 3.3).
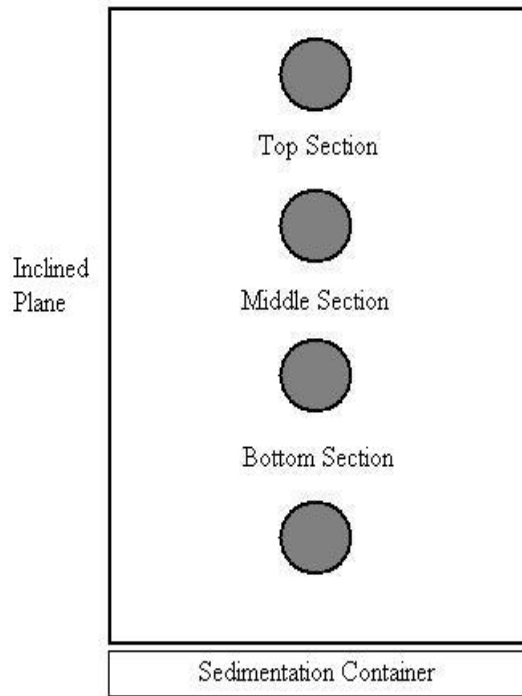
Figure 3.3: Schematic diagram of the sections of the plane for which erosion rate was determined.

Measurement of the erosion rate occurring between successive release points in an experiment was determined by solving for the following equations:

$$1 \qquad \frac{(|M1 - M2|)}{Bd} = Vp$$

For Equation 1, M1 is the mass of 2.5 ϕ particles eroded by an avalanche released from point A, M2 is the mass of 2.5 ϕ particles eroded by an avalanche released from point B, Bd is the bulk density of the particles used and Vp is the Volume picked up.

37

$$2 \qquad \frac{\left(\frac{Vp}{Mw}\right)}{L} = Te$$

In Equation 2, Mw is the mean flow width, L is 1cm length and Te is the thickness of particles eroded.

$$3 \qquad \frac{Te}{Dt} = Er$$

In Equation 3, Δt is the time it takes M1 to go from release point A to release point B and lastly, Er is the erosion rate with units of cm/sec.

The captured video frames, each representing 1/30 of a second, were retrieved with a digital frame grabber and saved as individual GIF images. Measurements of the propagating granular mass were taken directly from the frames by measuring the lateral spread at the top, middle and bottom of the mass, as well as the distance between the head and tail of a flow (Fig. 3.4). Due to geometrical distortions and time steps when the material of the flow was thinly spread, the edge of the flow was often difficult to ascertain. The error in the measurements of geometry and position of the flow is estimated to range between 1.0-2.5 cm. Geometry and position of the flow did not vary greatly between sequential frames therefore measurements were only taken from 5-10 selected frames per experiment.
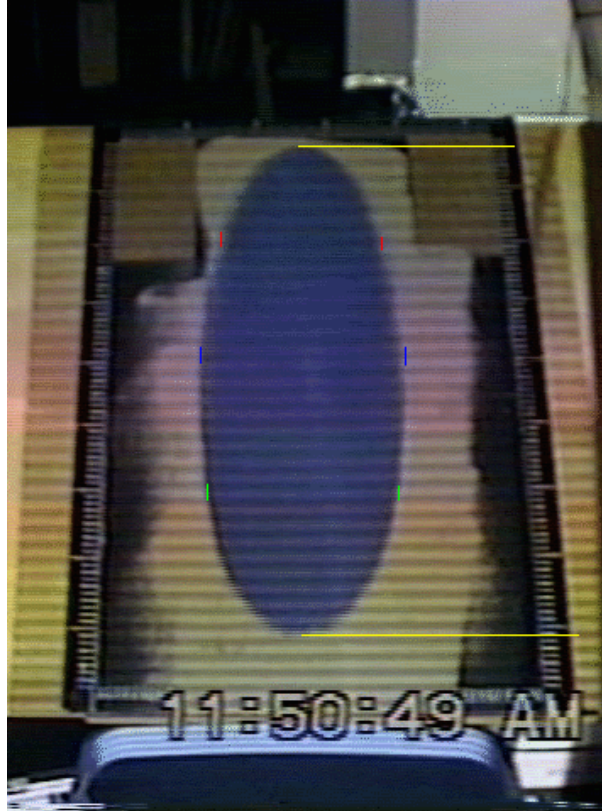
Figure 3.4: Image depicting how measurements were taken of the lateral spread (top = red lines, middle = blue lines, bottom = green lines) and the advance of the head and tail of the propagating flow (yellow lines).

3.3 Data and Analysis

For the purpose of validating the use of shields criteria to describe erosion of dry sediment, data was collected on the erosion, deposition, lateral spread and advance of the head and tail of dry granular flows. Experiments were performed by releasing sand from a cylinder down a rough inclined plane with a static deformable bed. Experiments were run at four different angles of inclination, 29.4°, 32.2°, 34.4° and 36.5°. The angles used in this experiment were chosen because they represent a range of angles that exist around the angle of repose and the angle of maximum stability. At each of these angles four runs were performed, each executed from a different release point. The first run was released near the top of the plane, the second from the top-middle, the third from the bottom-middle and the fourth near the bottom.

A typical experiment proceeded as follows: a layer of 2.5 ϕ sand was broadcast onto the inclined plane to form a uniformly thick static layer. Once the erodible bed was in position and stable the video was started and the operator placed the container flush to the erodible bed. The pre-weighed 2 ϕ sand was poured into the container, which was then removed in a fluid motion to avoid any unnecessary disturbance of the particles contained within. The head of the mass of released particles began to flow down the slope, as the tail remained stationary. As the mass flowed down the slope it spread laterally as well as downstream causing the mass to rapidly evolve into a teardrop shape. As propagation continued, the mass of solid particles constituting the avalanche changed as particles from the erodible bed were mobilized and entrained at the front of the flow, pushed to the rear and frequently deposited back on the bed. The avalanche mass also changed as a result of the deposition of 2 ϕ particles on the bed. Once the widest part of the teardrop shaped mass crossed the downstream edge of the inclined plane, the shape of the flowing material changed to that of an inverted, elongated horseshoe. This geometry held true for all experiments, the only change occurring in the intensity of blue each final outline maintained due to the amount of 2 ϕ particles that either deposited on the bed or flowed off the edge. The only exception to this geometry was in experiments performed at angles within the range of the basal friction angle, in which case, if the experiment was initiated sufficiently high on the inclined plane, the entire mass came to rest in a teardrop shape on the inclined plane. Once each run ended, material located in the sedimentation container was sieved into two masses representing blue 2 ϕ and tan 2.5 ϕ fractions. Each fraction was then weighed to determine how much of each particle size constituted the captured material. The mass of 2.5 ϕ particles eroded into the sedimentation container was used to determine an erosion gradient, which was subsequently used in conjunction with flow speed data to determine erosion rate.

3.4 Results and Discussion

Data on the rate of erosion occurring in avalanches in the downstream direction was derived from erosion gradient data collected from experiments initiated at four different angles of inclination. The data was then graphed to reveal any trends.

In Table 3.1, information is shown on the amount of 2 and 2.5 φ particles found in the sedimentation container after each run. For each angle of inclination tested in these experiments, the amount of 2 φ particles found in the sedimentation container increased as the position of the release point shifted lower on the inclined plane. This is due to the decreasing amount of space the 2 φ particles had to deposit on the inclined plane. For angles 29.4° and 32.2° the same increasing trend is exhibited for the amount of 2.5 φ particles found in the sedimentation container. However, for angles 34.4° and 36.5° the trend is exactly opposite, the amount of 2.5 φ particles found in the sedimentation container decreased as the position of the release point shifted lower on the inclined plane.

In Figure 3.5, Graphs A, B, C and D, the general trend shows that as the angle of the platform increases the general rate of erosion increases. Since the thickness of the flow layer decreases as the angle of the inclined plane increases this trend indicates that erosion, at any of the angles tested, is not occurring through the entire depth of the static layer. There does not appear to be any trend exhibited in the graphs on the rate at which the top, middle and bottom sections of the inclined plane are eroded. In Graph A, the rate of erosion measured in the top and middle sections is zero. Table 3.5 shows that no sediment reached the sedimentation container from avalanches initiated from release points located at the top, top-middle and bottom-middle of the plane. This indicates that the angle is within the range of the basal friction angle and that the avalanches were initiated sufficiently high on the plane so that the entire mass came to rest on the inclined plane. The avalanche released at the bottom of the plane did result in a small amount of erosion. In Graphs B, C and D, the top, middle and bottom sections each

experienced some amount of erosion. In Graphs B and D, the rate of erosion is greatest in the middle section of the plane whereas in Graph C, the rate of erosion increases as the release point shifts lower on the inclined plane.

Angle of Platform	Release Point	2 phi particles in bin (g)	2.5 phi particles in bin (g)	Erosion Rate (cm/s)
29.4	Top	0	0	Top Section: 0
	Top-Middle	0	0	Middle Section: 0
	Bottom-Middle	0	0	Bottom Section: 0.51
	Bottom	148.81	5.26	
32.2	Top	0	0	Top Section: 0.49
	Top-Middle	30.77	3.94	Middle Section: 2.01
	Bottom-Middle	202.89	24.13	Bottom Section: 0.54
	Bottom	366.82	18.45	
34.4	Top	188.36	41.7	Top Section: 0.01
	Top-Middle	234.84	41.77	Middle Section: 0.87
	Bottom-Middle	317.89	32.13	Bottom Section: 1.92
	Bottom	382.93	15.08	
36.5	Top	330.64	130.02	Top Section: 4.02
	Top-Middle	361.68	100.61	Middle Section: 4.45
	Bottom-Middle	383.58	64.47	Bottom Section: 3.84
	Bottom	405.47	30.56	

Table 3.1: Information on the amounts of 2 and 2.5 ϕ particles found in the sedimentation container after each run as well as the erosion rate calculated for each of the three sections per angle of inclination.

A

Angle 29.4

Erosion Rate (cm/s)

0.60
0.50
0.40
0.30
0.20
0.10
0.00

0.00   20.00   40.00   60.00   80.00

Distance Of Section Down Slope (cm)

- Top Section
- Middle Section
- Bottom Section

B

Angle 32.2

Erosion Rate (cm/s)

2.50
2.00
1.50
1.00
0.50
0.00

0.00   20.00   40.00   60.00   80.00

Distance Of Section Down Slope (cm)

- Top Section
- Middle Section

C

Angle 34.4

Erosion Rate (cm/s)

2.50
2.00
1.50
1.00
0.50
0.00

0.00   20.00   40.00   60.00   80.00

Distance Of Section Down Slope (cm)

- Top Section
- Middle Section

D

Angle 36.5

Erosion Rate (cm/s)

4.50
4.40
4.30
4.20
4.10
4.00
3.90
3.80
3.70
3.60

0.00   10.00   20.00   30.00   40.00   50.00   60.00

Distance Of Section Down Slope (cm)

- Top Section
- Middle Section

Figure 3.5: Graph of the rate of erosion occurring at the top, middle and bottom sections of an inclined plane as avalanches propagate down the plane at a range of angles.

3.5 Conclusions

The present research consisted of the collection of data on the geometric evolution and erosional characteristics of avalanches initiated down a rough inclined plane with a deformable bed at a variety of angles. The purpose of this data is to test the hypothesis that erosion can be incorporated into the Titan2D model by formulating criteria similar to Shield's stress criteria used in fluidized flow. The testing of this hypothesis is not included in this research. Information on the testing of this hypothesis and the results are reported in a paper in Appendix C (Nichita et al., 2004).

Chapter 4

Laboratory Granular Flow Experiments Using Photoelastic Discs

4.1 Introduction

Developing numerical models to simulate natural phenomena requires a system of validation. It is not always convenient or possible to use actual events to validate models that simulate behaviors such as particle flow and interaction. Laboratory experiments permit control over parameters such as material properties and bed geometries, which allow for easy comparison of flow theory with experiments.

Using photoelastic discs, Geng et al. (2003) were able to examine first-hand the complexity of static granular systems. The discs, used in a two-dimensional realization of static non-cohesive granular systems, provided Geng et al. (2003) the ability to study force distribution by observing filamentary stress/force networks within the granular systems. When the discs are placed between crossed polarizers and subjected to stress, the plane of the material's polarization is rotated, changing the amount of light passing through the material. The magnitude of the light allowed through is a function of the amount of force applied. In areas of great stress, very bright filamentary stress chains appear representing the paths along which the majority of force is carried. In areas of low stress dim filamentary stress chains may appear and in areas of no stress no stress chains will form. Geng et al. (2002) found that when a static granular system is subjected to an applied external force, the result is a complicated network of stress chains, in which only a small portion of the system's grains carry the burden of the force. The fluctuations of stress within the stress chains mean that the forces involved are not spatially homogeneous but localized, heterogeneous and irregular (Jaeger et al., 1996).

Geng et al. (2002) did not extend their work to systems in motion, such as granular avalanches. Due to the complex rheology of granular material, it is difficult to develop numerical equations that correctly describe avalanche behavior under rapid motion and large shearing in three dimensions. Because it is assumed that most of the shearing that occurs in an avalanche takes place in a thin layer near the bottom and that velocity may not vary appreciably over depth, the material behavior only needs to be described at the base. The concept of incorporating the rheology of granular material into a single term describing the frictional stress that develops at the interface between the flowing material and the basal surface is the fundamental nature of depth-averaging flow variables. When flow variables are depth-averaged there is an integration in the z-direction and the state of the flow becomes dependent only on the local values (ie., at a given x,y) of the flow variables.

Photoelastic discs were used as particles in two-dimensional granular flow experiments. Data collected from these experiments was used to assess the force distribution occurring within dynamic granular systems as well as to validate the use of depth-averaging flow variables inherent in the Titan2D model.

4.2 General Characteristics of the Experiment

4.2.1 Experiment Set Up

Laboratory experiments were conducted using photoelastic discs released onto an inclined smooth plastic plane. The plane measured 65 cm by 0.9 cm and was enclosed by two glass sheets. The angle of inclination of the plane could be controlled by adjusting the position of the top of the plane within the two glass sheets. Photoelastic sheets with a thickness of 0.645 ± 0.013 cm were purchased from Vishay Measurements Group, Inc. Discs measuring 1.09 cm by 0.645 ± 0.013 cm were punched from the photoelastic sheets using a 12 mm nickel-plated steel cork borer. The discs were then used as particles in two-dimensional realizations of granular flows. The discs were

detained behind a plastic gate situated at the top of the inclined plane and then instantaneously released down the plane (Fig. 4.1). To stop the discs from sticking to each other and reduce friction between the discs and the glass sheets, the discs were lubricated with a fine baby powder and the width of the plane (0.9 cm) was slightly larger then the width of the discs (0.645 ± 0.013 cm).

To capture and analyze the development of stress chains in the photoelastic disc flows the MotionPro high-speed digital imaging system was purchased from Redlake (Fig. 4.2). By combining mega-pixel resolution and CMOS imaging technology with powerful software, the PCI-based MotionPro system offered high-speed motion analysis on a PC. See Appendix E for the MotionPro system spec. sheet. The camera, affixed with a Vivitar 70–210 mm manual focus lens, was set to a resolution of 1280 by 1024 and a frame rate ranging from 125–250 frames per second. The camera depth was set to "Scaled Full 10-bit", to visualize a full spectrum of colors. The camera gain level was set to "1.0 - For Dark Scenes", to compensate for low lighting during the experiment.
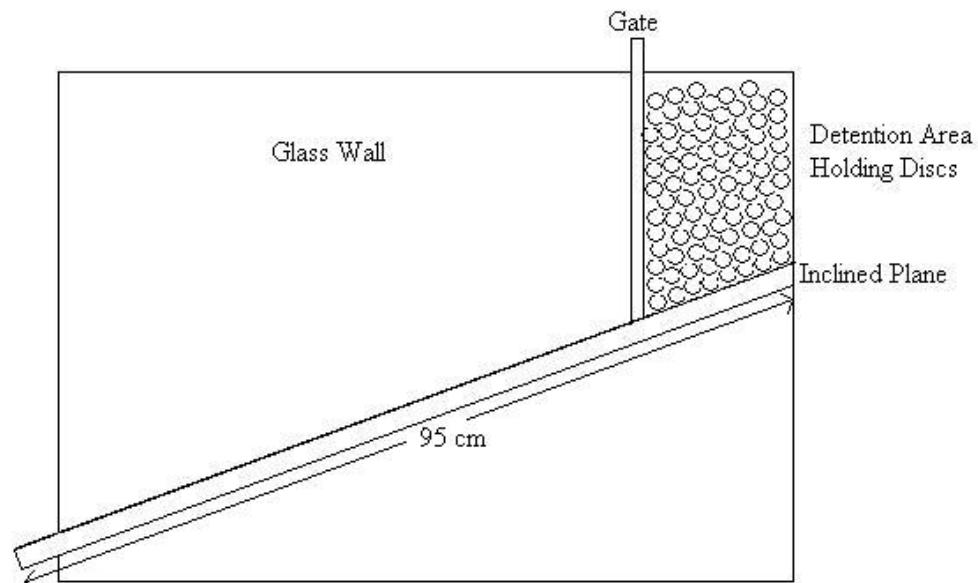
Figure 4.1: Schematic diagram of the glass enclosed inclined plane with discs detained behind the gate.

Figure 4.2: Image of the MotionPro high-speed digital imaging system components.

     To visualize the stress chains produced during the course of a flow, the discs were placed between crossed polarizers, one on each side of the enclosed plane.   A 61 cm by 49.5 cm polarized sheet purchased from Alight covered the glass wall nearest to the lights and the camera, attached with a circular polarizing lens, was positioned on the opposite side of the enclosed plane. Three Lowel, DP 1000W, 120V lamps were positioned behind the experimental set up for lighting. To diffuse the intensity of the light emitted, a thin sheet of opaque plastic with a pyramidal texture was placed between the light source and the enclosed plane (Fig. 4.3).
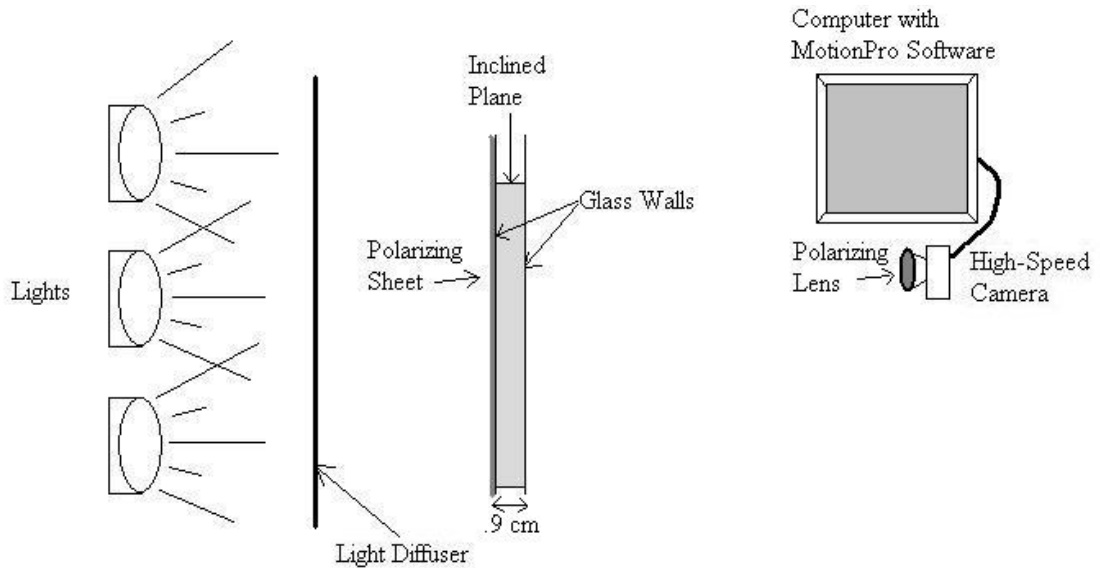
Figure 4.3: A side view schematic diagram of the experiment set-up.

4.2.2 Measurement Method

To capture each photoelastic disc flow, the MotionPro high-speed camera was positioned as close to the inclined plane as possible with minimum distance and angle dictated by the requirement that the entire flow zone from gated detention area to the end of the inclined plane be captured. The photoelastic disc flows were recorded by the camera at a rate of 125–250 frames per second. The frames recorded by the camera could either be played back like a movie or analyzed individually. The ability to analyze each frame individually was utilized to measure the stress chain orientations that developed as the discs interacted with one another during the course of the flow. For each frame that contained a visible stress chain the following characteristics were recorded: the angle of the platform and stress chain in relation to horizontal, the Δ angle between the angle of the chain and platform, the length of the chain and the number of discs involved.

4.3 Data and Analysis

For the purpose of validating the depth-averaging of flow variables inherent in the Titan2D model, data was collected on the orientation of stress chains that developed in photoelastic discs used in two-dimensional granular flow experiments. Experiments were run at four different angles of inclination, 18°, 22°, 28° and 30°. The angles used in this experiment were chosen because they represent a range of angles that exist around the angle of repose and the angle of maximum stability. However, the highest angle used was limited due to the size of the experimental set-up. As the angle of the inclined plane increased, the number of discs that could fit behind the gate decreased. To maintain a flow that could achieve a thickness of at least three discs, the angle of the incline could not be set above ~ 30°.

A typical experiment proceeded as follows: the inclination of the plane was adjusted to the desired angle and the detention area was filled with discs (the flat sides of the disks parallel to the glass). The lights and camera were positioned and turned on and the polarizing lens on the camera was adjusted for maximum visualization of the stress chains. The desired frame rate, resolution, camera depth and gain were entered into the MotionPro software and the software record function connected to the camera was activated. To initiate a flow the gate was lifted releasing the discs detained behind it. As the discs were released they began tumbling down the slope. At first the flow was thin (one or two discs thick) but as discs continued to move out from the detention area they began to tumble over one another increasing flow thickness to an average of 3-4 discs thick. As the run neared completion, the number of discs moving down the slope decreased causing the flow to thin. During the course of the flow as the discs interacted with one another stress chains developed and could be seen on the computer monitor (Fig. 4.4). Images with visible stress chains were then analyzed to assess stress chain orientation. Stress chains that developed within the detention area as a result of the discs dropping down to become part of the flow were not included in the measurements. Only stress chains that developed as a result of discs flowing over one another as they moved down the inclined plane were assessed. This data was then used

50

to determine the viability of depth averaging flow variables in numerical models of granular flows.

The main method of analysis is a quantitative analysis of stress chain orientation in relation to the angle of the platform. Measurements of the Δ angle between the angle of each stress chain measured and the angle of the platform at which the stress chain occurred were made. Stress chain angles that are non-vertical correspond to a Δ angle that is closer to 0°. The presence of mostly non-vertical stress chains would signify that stresses are spread out and that depth-averaging of flow variables is not suitable because a portion of what is going on at a given (x,y) might be related to something going on at another (x,y). Stress chain angles that are vertical correspond to a Δ angle that is closer to 90°. The presence of mostly vertical stress chains would signify that the use of depth-averaging equations in the Titan2D model is valid.

Figure 4.4: Image captured by the MotionPro high-speed camera, of a stress chain that developed in a photoelastic disc flow experiment.

4.4 Results and Discussion

Data on the characteristics of particle interaction in granular flows as represented by stress chains visible in photoelastic discs was collected from two-dimensional realizations of granular flows initiated at four different angles of inclination. The variables measured were the angle of the platform and stress chain in relation to horizontal, the Δ angle between the angle of the chain and the angle of the platform and the length of the chain. This data was graphed to reveal any general trends. Generally the magnitude of stress occurring as the discs interacted with one another was below the level that excites the discs to glow therefore the stress chains that were visible and analyzed represent the hardest impacts carrying the greatest stresses.

In Figures 4.5 and 4.6 both the graphs exhibit significant scatter but there is one general trend. As the length of the stress chain decreases, its angle with respect to horizontal becomes closer to perpendicular.
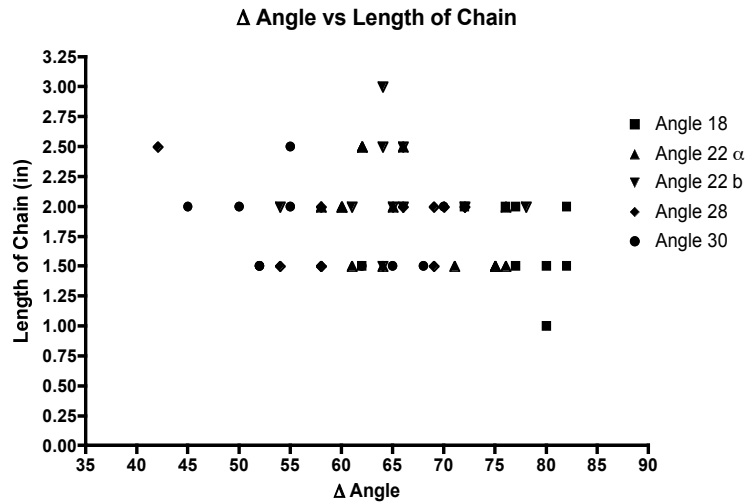
Figure 4.5: Graph of the stress chain extent in relation to the Δ angle occurring between each stress chain and the angle of the platform at which the experiment was run.

Angle of Chain vs Length of Chain
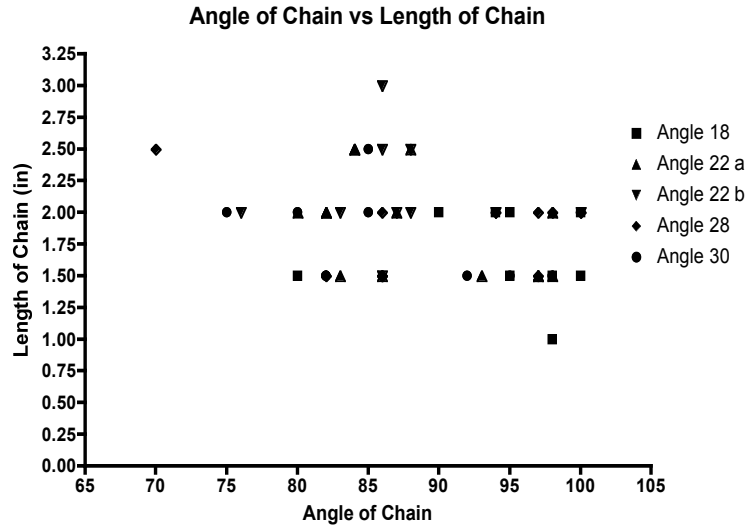
Figure 4.6: Graph of the stress chain extent in relation to the angle of the stress chain to horizontal. Angles greater than 90° signify the stress chain is oriented more perpendicular to the flow direction. Angles less than 90° signify the stress chain is oriented in the flow direction.

In Figure 4.7, the general trend exhibited in the graph is for the stress chain length to remain under 2.5 inches or 5 discs long regardless of the platform angle. Since flows rarely exceed 4-5 discs thick, except near the gate as the discs leave the detention area, there is minimal opportunity for the extent of a stress chain to grow much longer then 2.0-2.5 inches.

Mean and Standard Error Mean

53
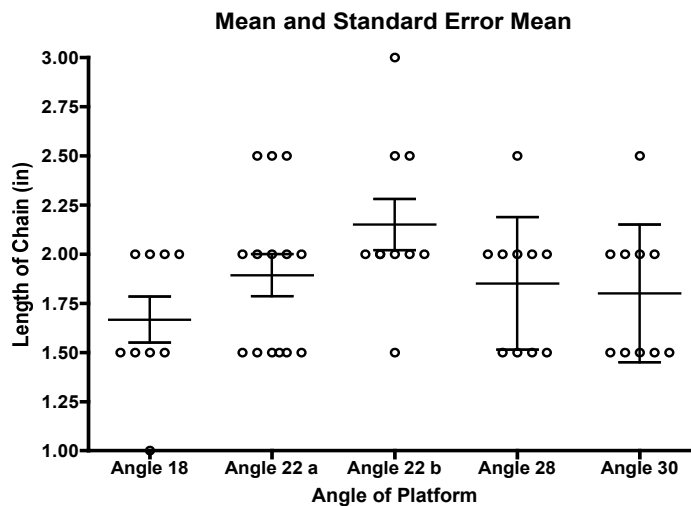
Figure 4.7: Graph of the stress chain extent distribution in relation to the angle of the platform at which the experiment was run. Mean and standard error of the mean bars are shown.

In Figure 4.8, the graph shows that as the angle of the platform increases the Δ angle between the stress chain and the platform decreases indicating that the angle of the stress chain becomes more aligned with the flows direction as the angle of the platform increases.

Mean and Standard Error Mean
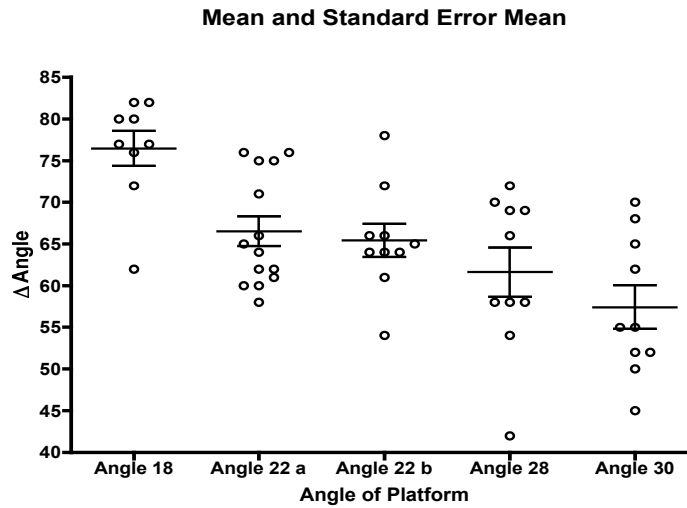
Figure 4.8: Graph of the Δ angle occurring between each stress chain and the angle of the platform at which the experiment was run in relation to the angle of the platform. Mean and standard error of the mean bars are shown.

Tables 4.1 and 4.2 contain information on the Δ angles measured for photoelastic disc flows run at the lowest and highest angles chosen for these experiments. The results show that for the platform angles used in these experiments the Δ angle is always closer to 90° than to 0°. This signifies that the use of depth-averaging flow variables to describe granular flows within the range of angles tested is valid. However, the trend exhibited in these tables as well as in Figure 4.8 shows that as the angle of the platform increases the Δ angle decreases. This indicates that theoretically, as the platform angle increases above a certain angle the general angle of the stress chains that develop will be closer to the angle of the platform. When stress chains develop near the angle of the platform, the Δ angle will be closer to 0° than to 90°, which means that depth-averaging flow variables is no longer valid.

54

Angle of the Platform	Angle of the Stress Chain	Δ Angle	Vertical / Non-Vertical
18	90	72	Vertical
18	100	82	Vertical
18	100	82	Vertical
18	98	80	Vertical
18	94	76	Vertical
18	95	77	Vertical
18	95	77	Vertical
18	80	62	Vertical
18	98	80	Vertical
Average	94.4	76.4	Vertical

Table 4.1: A table of the stress chain characteristics for a photoelastic disc flow initiated at an angle of 18°.

Angle of the Platform	Angle of the Stress Chain	Δ Angle	Vertical / Non-Vertical
30	98	68	Vertical
30	100	70	Vertical
30	85	55	Vertical
30	85	55	Vertical
30	80	50	Vertical
30	95	65	Vertical
30	82	52	Vertical
30	75	45	Vertical
30	82	52	Vertical
30	92	62	Vertical
Average	87.4	57.4	Vertical

Table 4.2: A table of the stress chain characteristics for a photoelastic disc flow initiated at an angle of 30°.

4.5 Conclusions

The present research is a quantitative analysis of the stress chains that develop and the characteristics they exhibit as a result of the interaction between photoelastic discs released down an inclined plane at a variety of angles. The results show that stress chains that develop at platform angles within the range of those tested (18°-30°) are oriented nearly vertical in relation to the angle of the platform. This indicates that the depth-averaging of flow variables inherent in the Titan2D model provides adequate fidelity to the rheology of avalanches initiated down angles within, or lower than, the range of angles tested. The validity of depth-averaging flow variables at angles greater than the range tested in this research should be investigated in future research.

Chapter 5

Conclusions

In chapters 1, 2 and 3 experiments were presented to test the strengths and limitations of the numerical granular flow model, Titan2D. In the first experiment, experimental and numerical data was gathered on the geometric evolution, position and timing of dry granular avalanches initiated down a smooth inclined plane. To explore the capability of the Titan2D model to simulate dry granular flows down smooth inclined planes the data was qualitatively and quantitatively compared. The results suggest that the Titan2D model, in general, provides a good description of several characteristics of real, small-scale physical flows and is a useful tool in simulating dry granular avalanches down smooth inclined beds. Discrepancies arose due to inaccuracies involved in defining the flow edge as well as a divergence of the physics defined in the flow model from those expressed in the experiments.

In the second experiment, data was gathered to aid in formulating criteria, similar to Shield's stress criteria, which would enable the description of erosion to be incorporated into the Titan2D model. Although the testing and results of this hypothesis are not included in this research, two significant observations were made regarding the propagation of avalanches down erodible beds. The first trend observed was that the general rate of erosion increased as the angle of the inclined plane increased. Since the thickness of the flow layer decreases as the angle of the inclined plane increases this trend indicates that erosion, at any of the angles tested, is not occurring through the entire depth of the static layer. The second trend observed was that erosion rate is not a monotonic function of the downstream distance an avalanche has traveled.

In the third experiment, force distribution seen within dynamic granular systems was analyzed to collect data suitable for assessing the validity of depth-averaging flow

variables. By analyzing the orientation of stress chains that developed in photoelastic discs (used as particles in two-dimensional granular flows) it was observed that the mean angle achieved by the stress chains analyzed was vertical with respect to horizontal. This implies that depth-averaging flow variables to describe avalanches initiated at inclines within, or lower than, the range of angles tested in this research (18°-30°) is valid. As well, because the stress chains that were analyzed represent the hardest impacts, the mean vertical orientation of the stress chains also implies that the strongest stress chains arise due to lithostatic stress exerted on the pile. Another trend observed was that as the angle of the inclined plane increased, the stress chains that developed became orientated more parallel to the slope. This is an important observation due to the theoretical possibility that at some angle greater than 30° the Δ angle should be closer to 0° than 90°, at which point depth-averaging flow variables would no longer be considered a viable option. More research needs to be conducted on the force distributions observed in avalanches initiated at angles greater than 30° to determine the validity of depth-averaging flow variables at these angles.

The results from each of the experiments strongly suggest that the Titan2D program provides adequate fidelity to several characteristics of real, small-scale physical flows. However, the model currently accounts only for the deformation of solid material consisting of a uniform particle size. Actual geophysical events involve much more complex and unique heterogeneous mixtures of materials than the particles used in these experiments. Enabling it to account for interstitial fluid and multiple particle sizes in a single flow would enhance the model. Also, the Titan2D program would benefit from a detailed comparison of simulations to field data collected from large-scale geophysical events.

This research has provided an improved and strengthened understanding of the ability of the Titan2D model equations and numerical solver to simulate dry granular flows. The Titan2D tool could prove extremely useful to geoscientists and civil protection authorities in the risk assessment and mitigation of hazards due to dry debris and avalanche flows.

Appendix A

Internal And Basal Friction Angle Data

Internal Friction Angle Data

Inclining Masonite Plane
37.8
37
36.8
36.9
37.4
38.1
37.3
38.1
38.3
38.2
37.8
36.1
37.9
36.2
36.1
37.5
37
37.2
37.6
38.8
37.4
36.1
36
38.2
35.7
36.5
38
37.2
38.1
37.6
Average: 37.3

Table A.1: Internal friction angle data for 2 ϕ sand. Data was collected from experiments performed by placing a pile of sand on a masonite plane and tilting the plane until internal movement was observed.

Basal Friction Angle Data

Inclining Masonite Plane and Block Of Plastic	Declining Masonite Plane and Pipet	Tilted Rectangular Container
18.8	2.75	34
19.3	29.2	35
16.4	30.15	36
Average: 18.2	28.9	36
	28.9	32
	28.7	33
	Average: 28.9	34
		35
		33
		36
		Average: 34.4
Average of the three experiments: 27		

Table A.2: Basal friction angle data for 2 ϕ sand. Data was collected in three different experiments.

Appendix B

Smooth Inclined Plane Data

Angle 37.4; Release Point = Top
Release Mechanism = Spherical Cap

Numerical: Distance between the head
and tail of a flow

Time(s)	Contour .001(cm)	Contour .0005(cm)	Contour .00025(cm)
0.00	4.59	4.59	4.59
0.03	6.12	6.76	7.91
0.33	15.56	25.26	29.91
0.63	*	17.48	52.94
0.93	4.72	15.05	32.78
1.23	6.00	7.21	9.18

Numerical: Lateral spread

Time(s)	Contour .001(cm)	Contour .0005(cm)	Contour .00025(cm)
0.00	4.08	4.08	4.59
0.03	6.18	6.37	7.65
0.33	10.32	14.02	17.71
0.63	*	12.36	21.73
0.93	15.93	23.19	26.76
1.23	22.68	25.36	28.04

Table B.1:
Lateral spread and distance between the tail and head of the flow data collected from simulated and observed flows. The simulated and observed flows were initiated from a spherical cap at the top of a smooth inclined plane at an angle 37.4°. The simulated data was collected for three defining edge pile height contours.

* Gaps in data represent an unreasonably low numerical output of −1.0 E+30.

Experiment A

Image	Width(cm)	Total Length(cm)	Time(s)
dgf1095	5	5	0.00
dgf1096	6.35	10.16	0.03
dgf1106	12.07	40.64	0.33
dgf1116	14.61	71.75	0.63
dgf1126	27.31	55.88	0.93
dgf1136	33.02	41.91	1.23

Experiment B

Image	Width(cm)	Total Length(cm)	Time(s)
dgf2025	5	5	0.00
dgf2026	6.35	10.16	0.03
dgf2036	13.34	40.6	0.33
dgf2046	15.86	73.03	0.63
dgf2056	24.13	47	0.93
dgf2066	36.83	39.37	1.23

Angle 37.4; Release Point = Middle
Release Mechanism = Spherical Cap

Numerical: Distance between the head
and tail of a flow

Time(s)	Contour .001(cm)	Contour .0005(cm)	Contour .00025(cm)
0.00	4.08	4.08	4.08
0.06	7.65	8.29	9.44
0.30	16.80	23.90	28.30
0.36	14.70	26.40	32.80
0.54	*	24.20	46.30
0.66	*	27.80	44.20
0.81	7.65	13.60	28.60
1.02	6.00	6.89	8.29
1.05	6.12	7.08	8.67

Numerical: Lateral spread

Time(s)	Contour .001(cm)	Contour .0005(cm)	Contour .00025(cm)
0.00	4.08	4.08	4.59
0.06	7.39	8.16	9.43
0.30	10.7	13.4	16.1
0.36	9.43	14.1	17.3
0.54	*	13.6	20.5
0.66	*	13.5	22.7
0.81	18.7	22.6	25.5
1.02	21.4	23.8	26.8
1.05	21.4	23.7	26.8

Table B.2:
Lateral spread and distance between the tail and head of the flow data collected from simulated and observed flows. The simulated and observed flows were initiated from a spherical cap from the middle of a smooth inclined plane at an angle 37.4°. The simulated data was collected for three defining edge pile height contours.

* Gaps in data represent an unreasonably low numerical output of –1.0 E+30.

Experiment A

Image	Width(cm)	Total Length(cm)	Time(s)
dgf31133	5	5	0.00
dgf31135	8.26	8.89	0.06
dgf31145	15.24	39.37	0.36
dgf31155	19.05	52.08	0.66
dgf31167	28.58	27.31	1.02

Experiment B

Image	Width(cm)	Total Length(cm)	Time(s)
dgf4150	5	5	0.00
dgf4152	8.26	6.99	0.06
dgf4161	13.97	45.72	0.30
dgf4169	15.24	57.16	0.54
dgf4178	24.77	33.03	0.81
dgf4186	26.67	25.4	1.05

Angle 37.4; Release Point = Bottom
Release Mechanism = Spherical Cap

Numerical: Distance between the head
and tail of a flow

Time(s)	Contour .001(cm)	Contour .0005(cm)	Contour .00025(cm)
0.00	4.59	4.59	4.59
0.09	9.25	10.33	11.74
0.21	16.07	18.24	21.18
0.36	19.26	25.00	27.75
0.48	9.18	18.11	22.90
0.63	6.51	7.02	10.59

Numerical: Lateral spread

Time(s)	Contour .001(cm)	Contour .0005(cm)	Contour .00025(cm)
0.00	4.08	4.08	4.59
0.09	8.47	9.30	11.21
0.21	11.09	12.55	14.91
0.36	9.68	14.78	17.97
0.48	16.95	18.92	21.54
0.63	18.22	20.45	22.68

Table B.3:
Lateral spread and distance between the tail and head of the flow data collected from simulated and observed flows. The simulated and observed flows were initiated from a spherical cap at the bottom of a smooth inclined plane at an angle 37.4°. The simulated data was collected for three defining edge pile height contours.

Experiment A

Image	Width(cm)	Total Length(cm)	Time(s)
dgf5179	5	5	0.00
dgf5182	8.89	8.89	0.09
dgf5186	12.07	20.96	0.21
dgf5191	10.8	22.87	0.36
dgf5195	15.24	13.97	0.48
dgf5200	16.51	9.53	0.63

Angle 40.1; Release Point = Top
Release Mechanism = Spherical Cap

Numerical: Distance between the head and tail of a flow

Time(s)	Contour .001(cm)	Contour .0005(cm)	Contour .00025(cm)
0.00	4.59	4.59	4.59
0.06	7.78	7.78	9.95
0.36	14.40	26.40	32.10
0.66	*	13.80	54.20
0.95	5.49	13.80	30.40
1.11	5.49	7.14	10.00
1.20	5.87	7.21	9.18

Numerical: Lateral spread

Time(s)	Contour .001(cm)	Contour .0005(cm)	Contour .00025(cm)
0.00	4.08	4.08	4.59
0.06	7.26	7.77	9.43
0.36	9.68	14.40	18.00
0.66	*	11.90	21.90
0.95	18.10	23.80	26.80
1.11	22.90	25.50	28.00
1.20	22.70	25.50	28.00

Table B.4:
Lateral spread and distance between the tail and head of the flow data collected from simulated and observed flows. The simulated and observed flows were initiated from a spherical cap at the top of a smooth inclined plane at an angle 40.1°. The simulated data was collected for three defining edge pile height contours.

* Gaps in data represent an unreasonably low numerical output of $-1.0 \text{ E}+30$.

Experiment A

Image	Width(cm)	Total Length(cm)	Time(s)
dgf7140	5	5	0.00
dgf7142	6.99	10.16	0.06
dgf7152	13.34	44.45	0.36
dgf7162	15.88	69.22	0.66
dgf7172	25.4	50.81	0.95
dgf7181	52.07	31.75	1.20

Experiment B

Image	Width(cm)	Total Length(cm)	Time(s)
dgf8494	5	5	0.00
dgf8496	8.26	8.89	0.06
dgf8506	13.97	46.99	0.36
dgf8516	15.86	67.32	0.66
dgf8526	31.75	48.27	0.95
dgf8531	53.34	39.37	1.11

Angle 40.1; Release Point = Middle
Release Mechanism = Spherical Cap

Numerical: Distance between the head and tail of a flow

Time(s)	Contour .001(cm)	Contour .0005(cm)	Contour .00025(cm)
0.00	4.08	4.08	4.08
0.06	7.65	8.29	9.44
0.24	17.10	20.30	23.50
0.27	17.10	22.20	25.20
0.42	6.89	26.90	36.50
0.48	*	25.90	41.30
0.61	*	24.60	39.80
0.69	6.12	15.20	32.70
0.81	7.14	10.60	15.90
0.87	6.25	8.29	11.20

Numerical: Lateral spread

Time(s)	Contour .001(cm)	Contour .0005(cm)	Contour .00025(cm)
0.00	4.08	4.08	4.59
0.06	7.39	8.16	9.43
0.24	11.50	13.50	15.90
0.27	11.60	13.60	16.80
0.42	6.37	15.20	19.60
0.48	*	14.50	20.20
0.61	*	16.10	23.10
0.69	10.70	20.80	24.70
0.81	20.60	24.20	26.90
0.87	21.40	24.40	27.50

Table B.5: Lateral spread and distance between the tail and head of the flow data collected from simulated and observed flows. The simulated and observed flows were initiated from a spherical cap from the middle of a smooth inclined plane at an angle 40.1°. The simulated data was collected for three defining edge pile height contours.

* Gaps in data represent an unreasonably low numerical output of −1.0 E+30.

Experiment A

Image	Width(cm)	Total Length(cm)	Time(s)
dgf9433	5	5	0.00
dgf9435	7.62	8.89	0.06
dgf9441	12.7	26.67	0.24
dgf9447	14.61	46.36	0.42
dgf9453	20.96	38.1	0.61
dgf9460	22.86	29.21	0.81

Experiment B

Image	Width(cm)	Total Length(cm)	Time(s)
dgf10339	5	5	0.00
dgf10341	6.35	7.62	0.06
dgf10348	13.34	25.4	0.27
dgf10355	16.51	48.9	0.48
dgf10362	21.59	31.76	0.69
dgf10368	28.58	29	0.87

Angle 43.6; Release Point = Top
Release Mechanism = Spherical Cap

Numerical: Distance between the head and tail of a flow

Time(s)	Contour .001(cm)	Contour .0005(cm)	Contour .00025(cm)
0.00	4.59	4.59	4.59
0.06	7.91	8.29	9.95
0.36	12.00	27.00	31.70
0.66	*	18.50	40.30
0.81	8.04	14.40	20.70
0.87	8.16	11.40	14.90
0.99	6.51	7.40	8.61
1.02	6.51	7.53	9.06

Numerical: Lateral spread

Time(s)	Contour .001(cm)	Contour .0005(cm)	Contour .00025(cm)
0.00	4.08	4.08	4.59
0.06	7.39	7.77	9.43
0.36	9.30	15.20	18.20
0.66	*	18.50	23.60
0.81	16.20	22.60	26.00
0.87	18.60	23.80	26.80
0.99	20.40	23.90	27.50
1.02	20.30	23.80	27.50

Table B.6: Lateral spread and distance between the tail and head of the flow data collected from simulated and observed flows. The simulated and observed flows were initiated from a spherical cap at the top of a smooth inclined plane at an angle 43.6°. The simulated data was collected for three defining edge pile height contours.

* Gaps in data represent an unreasonably low numerical output of $-1.0\ E+30$.

Experiment A

Image	Width(cm)	Total Length(cm)	Time(s)
dgf131356	5	5	0.00
dgf131358	8.26	10.16	0.06
dgf131368	15.24	38.1	0.36
dgf131378	19.05	54.62	0.66
dgf131385	36.83	44.45	0.87
dgf131390	45.72	46.99	1.02

Experiment B

Image	Width(cm)	Total Length(cm)	Time(s)
dgf14154	5	5	0.00
dgf14156	7.62	8.89	0.06
dgf14166	16.51	39.37	0.36
dgf14176	25.4	53.35	0.66
dgf14181	29.85	41.28	0.81
dgf14187	33.02	39.37	0.99

Angle 43.6; Release Point = Middle
Release Mechanism = Spherical Cap

Numerical: Distance between the head and tail of a flow

Time(s)	Contour .001(cm)	Contour .0005(cm)	Contour .00025(cm)
0.00	4.08	4.08	4.08
0.06	7.72	8.42	9.69
0.21	16.50	18.40	21.20
0.24	17.50	20.50	23.20
0.39	7.53	28.10	34.00
0.54	*	26.70	37.80
0.57	*	23.10	36.00
0.72	8.67	13.60	17.50

Numerical: Lateral spread

Time(s)	Contour .001(cm)	Contour .0005(cm)	Contour .00025(cm)
0.00	4.08	4.08	4.59
0.06	7.39	8.16	9.43
0.21	11.10	12.90	15.50
0.24	11.30	13.60	15.90
0.39	6.37	15.20	19.00
0.54	*	15.50	21.40
0.57	*	18.50	22.60
0.72	17.70	22.50	25.20

Experiment A

Image	Width(cm)	Total Length(cm)	Time(s)
dgf151462	5	5	0.00
dgf151464	8.26	8.26	0.06
dgf151470	13.97	27.31	0.24
dgf151475	17.15	43.19	0.39
dgf151480	24.77	33.66	0.54
dgf151486	34.29	29.85	0.72

Experiment B

Image	Width(cm)	Total Length(cm)	Time(s)
dgf16334	5	5	0.00
dgf16336	7.62	8.26	0.06
dgf16341	11.43	22.86	0.21
dgf16347	15.88	42.55	0.39
dgf16353	18.42	34.3	0.57
dgf16358	27.94	31.12	0.72

Table B.7: Lateral spread and distance between the tail and head of the flow data collected from simulated and observed flows. The simulated and observed flows were initiated from a spherical cap from the middle of a smooth inclined plane at an angle 43.6°. The simulated data was collected for three defining edge pile height contours.

* Gaps in data represent an unreasonably low numerical output of −1.0 E+30.

Angle 43.6; Release Point = Bottom
Release Mechanism = Spherical Cap

Numerical: Distance between the head and tail of a flow

Time(s)	Contour .001(cm)	Contour .0005(cm)	Contour .00025(cm)
0.00	4.59	4.59	4.59
0.06	7.91	8.29	9.18
0.18	14.92	16.46	18.75
0.27	18.50	21.81	24.43
0.30	17.99	22.07	24.30
0.39	10.08	17.99	21.30
0.51	7.02	8.42	10.52

Numerical: Lateral spread

Time(s)	Contour .001(cm)	Contour .0005(cm)	Contour .00025(cm)
0.00	4.08	4.08	4.59
0.06	7.39	8.16	9.43
0.18	10.96	12.30	14.53
0.27	11.60	13.89	16.44
0.30	11.34	14.40	17.59
0.39	16.18	17.97	19.88
0.51	18.48	20.13	23.45

Table B.8: Lateral spread and distance between the tail and head of the flow data collected from simulated and observed flows. The simulated and observed flows were initiated from a spherical cap at the bottom of a smooth inclined plane at an angle 43.6°. The simulated data was collected for three defining edge pile height contours.

Experiment A

Image	Width(cm)	Total Length(cm)	Time(s)
dgf17128	5	5	0.00
dgf17130	7.62	7.62	0.06
dgf17134	12.07	17.15	0.18
dgf17137	13.34	22.87	0.27
dgf17141	17.15	12.71	0.39
dgf17145	20.23	12.7	0.51

Experiment B

Image	Width(cm)	Total Length(cm)	Time(s)
dgf18294	5	5	0.00
dgf18296	8.26	8.89	0.06
dgf18300	12.7	18.42	0.18
dgf18304	13.34	21.6	0.30
dgf18307	24.77	13.97	0.39
dgf18311	20.32	13.97	0.51

Angle 23.9
Release Mechanism = Cylinder

Numerical: Distance between head and tail of a flow

Time(s)	Contour .001(cm)	Contour .0005(cm)	Contour .00025(cm)
0	9.69	9.69	10.2
0.06	15.3	15.3	16.8
0.18	20.9	26	26
0.3	26	28.1	34.2
0.42	26	28.1	34.2
0.54	26	28.1	34.2
0.6	26	28.1	34.2

Table B.9: Lateral spread and distance between the tail and head of the flow data collected from simulated and observed flows. The simulated and observed flows were initiated from a cylinder at the top of a smooth inclined plane at an angle 23.9°. The simulated data was collected for three defining edge pile height contours.

Numerical: Lateral spread

Time(s)	Contour .001(cm)	Contour .0005(cm)	Contour .00025(cm)
0	10.2	10.2	10.2
0.06	15.3	15.3	18.4
0.18	24.5	26.5	32.6
0.3	26.5	29.6	32.6
0.42	26.5	32.6	32.6
0.54	26.5	32.6	36.7
0.6	26.5	32.6	36.7

Experiment A

Image	Width(cm)	Total Length(cm)	Time(s)
bgf239a548	10.5	10.5	0
bgf239a550	10.8	16.51	0.06
bgf239a554	16.51	26.04	0.18
bgf239a558	19.69	38.1	0.3
bgf239a562	20.96	45.72	0.42
bgf239a566	20.32	50.8	0.54
bgf239a568	20.32	53.34	0.6

Experiment B

Image	Width(cm)	Total Length(cm)	Time(s)
bgf239b330	10.5	10.5	0
bgf239b332	10.16	16.51	0.06
bgf239b336	15.88	24.13	0.18
bgf239b340	19.05	33.66	0.3
bgf239b344	20.96	42.55	0.42
bgf239b348	20.96	45.72	0.54
bgf239b350	22.86	50.8	0.6

Angle 31.8
Release Mechanism = Cylinder

Numerical: Distance between the head and tail of a flo

Time(s)	Contour .001(cm)	Contour .0005(cm)	Contour .00025(cm)
0.00	9.69	9.69	10.20
0.03	12.50	12.80	12.80
0.33	41.10	44.10	48.50
0.63	62.60	78.80	81.60
0.93	62.10	74.90	78.20
1.23	13.10	48.50	57.70
1.53	14.90	15.60	24.70
1.83	16.50	17.30	19.90
2.13	17.50	19.60	21.40
2.43	17.70	19.60	23.00
2.73	18.10	21.90	25.50
2.85	19.10	21.90	25.50
2.94	19.10	21.90	25.50

Table B.10: Lateral spread and distance between the tail and head of the flow data collected from simulated and observed flows. The simulated and observed flows were initiated from a cylinder at the top of a smooth inclined plane at an angle 31.8°. The simulated data was collected for three defining edge pile height contours.

Numerical: Lateral spread

Time(s)	Contour .001(cm)	Contour .0005(cm)	Contour .00025(cm)
0.00	10.20	10.20	10.20
0.03	12.20	12.50	13.50
0.33	29.40	33.40	38.20
0.63	29.70	37.00	42.20
0.93	44.00	45.60	46.50
1.23	45.10	46.30	47.30
1.53	44.60	45.80	47.30
1.83	44.10	45.50	46.50
2.13	43.80	45.40	46.50
2.43	43.30	45.20	46.50
2.73	43.10	45.00	46.40
2.85	43.10	45.00	46.40
2.94	42.80	45.00	46.60

Experiment A

Image	Width(cm)	Total Length Max(cm)	Total Length Min(cm)	Time(s)
bgf318a517	10.5	10.5	10.5	0.00
bgf318a518	10.8	16.51	16.51	0.03
bgf318a528	28.58	41.28	41.28	0.33
bgf318a538	27.31	80.01	80.01	0.63
bgf318a548	31.75	102.24	102.24	0.93
bgf318a558	28.58	113.03	113.03	1.23
bgf318a568	26.67	113.67	113.67	1.53
bgf318a578	20.32	97.8	97.8	1.83

```
bgf318a588    17.78        83.83         83.83        2.13
bgf318a598    19.69        67.32         67.32        2.43
bgf318a608    31.12        49.54         49.54        2.73
bgf318a615    33.02        45.73         44.46        2.94
```

Experiment B

Image	Width(cm)	Total Length(cm)	Time(s)
bgf318b307	10.5	10.5	0.00
bgf318b308	12.7	15.24	0.03
bgf318b318	27.94	42.55	0.33
bgf318b328	27.94	81.28	0.63
bgf318b338	25.4	102.87	0.93
bgf318b348	22.86	107.95	1.23
bgf318b358	21.59	111.13	1.53
bgf318b368	17.78	106.05	1.83
bgf318b378	17.78	88.91	2.13
bgf318b388	19.05	67.32	2.43
bgf318b398	29.21	47	2.73
bgf318b402	34.29	43.19	2.85

Angle 38.5
Release Mechanism = Cylinder

Numerical: Distance between the head and tail of a flow

Time(s)	Contour .001(cm)	Contour .0005(cm)	Contour .00025(cm)
0.00	9.69	9.69	10.20
0.03	12.10	12.80	13.50
0.21	31.20	33.20	37.50
0.24	34.60	36.90	41.60
0.39	51.80	56.90	59.70
0.45	55.60	64.70	67.90
0.57	69.40	75.90	78.60
0.66	67.00	75.10	78.30
0.75	55.10	68.40	73.00
0.87	24.40	50.60	58.30
0.93	22.30	38.70	47.60
1.08	14.50	19.30	21.30
1.11	13.60	16.60	18.00
1.29	15.10	16.50	17.60
1.44	15.90	17.50	18.60

Table B.11: Lateral spread and distance between the tail and head of the flow data collected from simulated and observed flows. The simulated and observed flows were initiated from a cylinder at the top of a smooth inclined plane at an angle 38.5°. The simulated data was collected for three defining edge pile height contours.

Numerical: Lateral spread

Time(s)	Contour .001(cm)	Contour .0005(cm)	Contour .00025(cm)
0.00	10.20	10.20	10.20
0.03	12.20	12.50	13.50
0.21	27.70	29.30	34.70
0.24	29.10	31.90	35.70
0.39	33.10	37.00	41.50
0.45	33.40	38.90	44.10
0.57	29.10	41.20	45.10
0.66	35.00	45.00	48.20
0.75	43.70	48.30	49.50
0.87	48.90	50.10	50.30
0.93	50.10	50.30	50.30
1.08	49.70	50.20	50.30
1.11	49.70	50.20	50.30
1.29	49.40	50.00	50.30
1.44	49.30	50.00	50.30

Experiment A

Image Time(s)	Width(cm)	Total Length Max(cm)	Total Length Min(cm)	
bgf385a837	10.5	10.5	10.5	0.00
bgf385a838	11.5	15.5	15.5	0.03
bgf385a844	23	29.5	29.5	0.21
bgf385a850	28	54.5	54.5	0.39

```
bgf385a856      28.5        80          80          0.57
bgf385a862      28          86          86          0.75
bgf385a868      24          72          72          0.93
bgf385a874      20          54          54          1.11
bgf385a880      61          34          34          1.29
bgf385a885      61          34          31          1.44
```

Experiment B

Image	Width(cm)	Total Length Max(cm)	Total Length Min(cm)	Time(s)
bgf385b361	10.5	10.5	10.5	0.00
bgf385b362	12.5	15	15	0.03
bgf385b369	26.5	36	36	0.24
bgf385b376	31	68.5	68.5	0.45
bgf385b383	30.5	89	89	0.66
bgf385b390	26	85.5	85.5	0.87
bgf385b397	18	71	71	1.08
bgf385b409	61	32	28	1.44

Angle 44.3
Release Mechanism = Cylinder

Numerical: Distance between the head and tail of a flo

Time(s)	Cwontour .001(cm)	Contour .0005(cm)	Contour .00025(cm)
0.00	9.69	9.69	10.20
0.03	11.86	12.76	12.76
0.24	37.25	38.59	40.57
0.45	54.72	67.61	70.22
0.66	45.03	60.47	64.93
0.87	23.98	26.34	28.45
0.99	14.10	15.88	17.22
1.05	14.03	16.33	18.37

Numerical: Lateral spread

Time(s)	Contour .001(cm)	Contour .0005(cm)	Contour .00025(cm)
0.00	10.20	10.20	10.20
0.03	12.23	12.49	13.51
0.24	29.95	32.24	35.68
0.45	35.30	43.96	46.83
0.66	47.15	50.34	50.34
0.87	50.34	50.34	50.34
0.99	49.95	50.27	50.34
1.05	49.70	50.21	50.34

Table B.12: Lateral spread and distance between the tail and head of the flow data collected from simulated and observed flows. The simulated and observed flows were initiated from a cylinder at the top of a smooth inclined plane at an angle 44.3°. The simulated data was collected for three defining edge pile height contours.

Experiment A

Image	Width(cm)	Total Length Max(cm)	Total Length Min(cm)	Time(s)
bgf443a596	10.5	10.5	10.5	0.00
bgf443a597	13	14	14	0.03
bgf443a604	23	30	30	0.24
bgf443a611	30	60.5	60.5	0.45
bgf443a618	32.5	78	78	0.66
bgf443a625	32.5	48.5	48.5	0.87
bgf443a631	61	40	22.5	1.05

Experiment B

Image	Width(cm)	Total Length Max(cm)	Total Length Min(cm)	Time(s)
bgf443b389	10.5	10.5	10.5	0.00
bgf443b390	13	14.5	14.5	0.03
bgf443b397	25	38	38	0.24
bgf443b404	33	68.5	68.5	0.45
bgf443b411	30.5	66	66	0.66
bgf443b422	61	39	21.5	0.99

Appendix C

A Model of Erosional Volcanic Granular Flows

A Model of Erosional Volcanic Granular Flows

C. Nichita   M. Bursik   A. Patra   E.B. Pitman   B. Rupp   A. Webb

June 8, 2004

Corresponding author:

M. Bursik

Department of Geology

876 Natural Sciences Complex

University at Buffalo

Buffalo, NY 14260 USA

email: mib@buffalo.edu

fax: 716 645 3999

Abstract

Volcanic granular avalanches, such as some pyroclastic flows, debris avalanches and debris flows show pervasive evidence for erosion. We model the erosion process in such granular flows using some concepts borrowed from erosion by aqueous flows. The results of the model show good agreement with experimental data on erosion and deposition by laboratory granular flows, and also with example block and ash flows of Colima volcano, Mexico, although estimates of initial and final volume for pyroclastic flows in nature are error prone. The results suggest that erosion affects propagation considerably, with ramifications for average flow speed, and possibly other bulk flow parameters, such as inundation area and runout distance.

1 Introduction

Many types of geophysical mass flows can be classified as granular avalanches. Volcanoes in particular are a rich environment in which to observe a number of types of granular flows. While sedimentation from volcanic granular avalanches leaves sometimes spectacular deposits that have been the subject of intense study for the past half-century [4, 12], the effects of erosion are both more difficult to measure and generally less spectacular in appearance.

1

Pervasive evidence for scour beneath pyroclastic flows does exist, although eroded volumes are difficult to estimate. Evidence for erosion includes striae and polish by pyroclastic flows and avalanches, similar to features resulting from glacier flow, as well as larger scour channels [2, 1]. Ui et al. [22] argued that significant amounts of slope talus were eroded during the Unzen block and ash flow eruptions of 1991-1995. Saucedo et al. [17, 18] argued that erosion was necessary to the increase in block and ash flow runout distance observed over the course of the April, 1991, sequence of Fuego de Colima. Voight et al. [23] showed that the Boxing Day volcanic debris avalanche of Soufriere Hills volcano bulked by nearly a factor of two with slope talus. Some debris flows start as water floods and therefore they obtain all their particle load during transport downslope. Even debris flows that start as granular avalanches can bulk by a factor of three due to erosion during transport [20].

No model exists for volcanic granular avalanches that incorporates erosion [7, 23]. Empirical correlations show however that there is a known correlation between runout distance or apparent friction angle and depth or mass of flowing debris [12]. It is also intuitively clear that basal shear stresses at slope angles between the maximum stability angle and the repose angle for clastic debris must result in erosion, since the repose angle is effectively the angle at which the slope debris can be eroded. Thus erosion must in some instances play a critical role in controlling flow dynamics.

The aim of this study is to present a model that simulates granular avalanches in which erosion as well as sedimentation cause significant changes in the mass and momentum during flow. We test the model against measurements from laboratory experiments and block and ash flows (small pyroclastic flows) at Colima volcano.

2 Model

The mathematical model is based on the Savage-Hutter theory for gravity driven thin-layer flows [19, 15]. The main feature of the current model is the analytical treatment of erosion as extra source terms (which are physically motivated) in the equations of motion. The equations of motion are solved with an adaptive-mesh, second-order finite-volume technique. In a first approximation we assume that changes in the topography of the basal surface due to erosion are small compared to the average flow depth. Therefore, we solve the equations of motion with the bed movement frozen, the net effect of erosion consisting only in the overall mass and momentum change of the flow.

The mathematical model is derived by vertically integrating the equations for a Mohr-Coulomb incompressible continuum and using the kinematic and kinetic boundary conditions at the bottom and the free surface. We assume that the interface between flowing granular material and the basal surface can move as a result of continuous exchange of sediment particles. The normal speed of the interface is assumed to be

2

equal to the erosion rate e_s.

In a local curvilinear system, the governing equations are a system of hyperbolic conservation laws, with source terms

$$\frac{\partial \mathbf{U}}{\partial t} + \frac{\partial \mathbf{F}}{\partial x} + \frac{\partial \mathbf{G}}{\partial y} = \mathbf{S} \tag{1}$$

where

$\mathbf{U} = (h, hv_x, hv_y)^t$,

$\mathbf{F} = (hv_x, hv_x^2 + 0.5k_{ap}g_z h^2, hv_x v_y)^t$,

$\mathbf{G} = (hv_y, hv_x v_y, hv_y^2 + 0.5k_{ap}g_z h^2)^t$, and $\mathbf{S} = (e_s, S_x, S_y)^t$ and where

$$S_x = -e_s v_x + g_x h - hk_{ap}\mathrm{sgn}(\frac{\partial v_x}{\partial y})\partial_y(g_z h)\sin\varphi_{int} - \frac{v_x}{\sqrt{v_x^2 + v_y^2}}\left[g_z h\left(1 + \frac{v_x}{r_x g_z}\right)\right]\tan\varphi_{bed}$$

$$S_y = -e_s v_y + g_y h - hk_{ap}\mathrm{sgn}(\frac{\partial v_y}{\partial x})\partial_x(g_z h)\sin\varphi_{int} - \frac{v_y}{\sqrt{v_x^2 + v_y^2}}\left[g_z h\left(1 + \frac{v_y}{r_y g_z}\right)\right]\tan\varphi_{bed}$$

In the above system, (h, hv_x, hv_y) are the depth-averaged height, and x and y momentum, $\mathbf{g} = (g_x, g_y, g_z)$ is the gravitational acceleration and (r_x, r_y) are the x and y radii of curvature. $\varphi_{int}, \varphi_{bed}$ are the internal and bed friction angles, $k_{ap} = 2\frac{1 \pm \left[1 - \cos^2\varphi_{int}(1 + \tan^2\varphi_{bed})\right]^{1/2}}{\cos^2\varphi_{int}} - 1$ are the active/passive lateral stress coefficients similar to relations from soil mechanics.

The presence of an erodible granular bed is known to increase the resistance force acting on the flowing material, since the roughness of the basal surface is significantly higher. We increase the basal friction angle by several degrees, to account for this modified drag force at the base. In addition, we assume that eroded particles must be accelerated to the speed of the flow, therefore the erosion terms in the momentum equations are treated as sinks. This seems to be consistent with our data on flow speed.

2.1 Empirical formula for the erosion rate

In the mathematical model we are presenting, we assume the bed level does not change in time, the net effect of erosion consisting in the mass and momentum change of the granular avalanche. The erosion rate is an empirical factor that describes the erosion of material at the basal surface. The physics at the interface is not yet completely understood, and several functional forms for the erosion rate can be found in the literature, formulae which are motivated by experimental observations([5, 11]). Generally accepted assumptions are that there is a threshold shear stress at the bed below which there is no erosion, and that the discharge increases monotonically with bed shear above the threshold. Takahashi et al. [21, 5] proposed a formula for erosion rate

$$e_s = \alpha\frac{c_e - c}{c_* - c_e}\frac{h}{d}v \tag{2}$$

3

where α is an experimental coefficient, v is the average velocity of the flow, c is the sediment concentration of debris by volume, c_* is the sediment concentration (by volume) of bed sediment (non-moving layer), c_e is the equilibrium sediment concentration (by volume) of debris corresponding to bed slope θ, h is the flow depth and d is the average grain size.

We propose a simpler expression for the erosion rate, based on a criterion for the basal shear stress. We define the effective shear stress to be $\tau_{eff} = T^\sigma|_{z=0} - T^0$ where $T^\sigma = \sqrt{T_{zx}^2 + T_{zx}^2}$ is the magnitude of the shear stress at a given point on the basal surface, and T^0 is a threshold shear stress similar to Shields stress from water flow studies. The shear stress may be evaluated from the Coulomb equation for basal sliding, and its x component is given by the formula

$$T_{zx} = -\frac{v_x}{\sqrt{v_x^2 + v_y^2}}\left[\rho g_z h\left(1 + \frac{v_x^2}{r_x g_z}\right)\right]\tan\varphi_{bed} \tag{3}$$

The y component of the shear stress is given by a similar relation, and it can be obtained by interchanging x and y in Equation 3.

To estimate the threshold shear, Parker et al. [14] wrote the equation for the equilibrium of forces acting on a particle in the boundary layer at the base that is being displaced and transported with the flow. They derived an explicit dependence of T^0 on the local slopes and on the threshold shear for a horizontal surface element, $T^0_{horizontal}$. We tested the formula derived by Parker et al. [14]:

$$T^0 = T^0_{horizontal}\cos\theta\max\left[1 - \frac{\tan\theta}{\tan\varphi_{int}}, 0\right]^n. \tag{4}$$

Here θ is the maximum slope angle and $\tan\theta = \sqrt{(\tan\theta_x)^2 + (\tan\theta_y)^2}$ where (θ_x, θ_y) are the local slope angles. n is treated as an empirical parameter to be determined by experiment. The formula, Eqn. [4] is consistent, in the sense that for slopes θ which are greater than the internal friction angle φ_{int}, there is no threshold stress for erosion, and in that the threshold stress achieves its maximum value for a surface element which is horizontal.

The effective shear stress may be used to define an associated shear velocity, $u_s = \left(\frac{\tau_{eff}}{\rho}\right)^{1/2} = \left(\frac{T^\sigma|_{z=0}-T^0}{\rho}\right)^{1/2}$. Using the associated shear velocity we define an erosion rate similar to the functional form of the Equation [2]:

$$e_s = \beta u_s = \beta\left(\frac{T^\sigma|_{z=0} - T^0}{\rho}\right)^{1/2} \tag{5}$$

For our model, the coefficient β as well as the power-law parameter n (Eq. 4) are assumed to be phenomenological constants. For more complex models, the value of β would be given by a functional form in which the dependence on flow depth, grain size, h_{eroded}/h_{total}, or on the elasticity coefficient describing the granular interaction at the base could be included. To avoid unphysical results, we exclude from our numerical computation erosion that is generated by a layer of material less than several particle diameters

4

thick, and also by flows moving at velocities smaller than a threshold speed. It is noteworthy that we do not explicitly model deposition, however deposition is inherent in the numerical computations. Whenever the flow velocity reduces significantly, the numerical computation of transport reduces to zero(i.e. mass flux from a cell to the next cell is negligible). This implies the mass is "deposited" at that location.

3   Tests

3.1   Experiments

Laboratory experiments were conducted using sand flows released on a masonite plane to which 36 grit sandpaper had been glued (Fig. 1a; Table 1). The masonite plane measured 95 cm × 60 cm. The plane was tilted at angles of 29.4–36.5 with an adjustable mount. Particles were playground sand grains sieved so that only the 2 and 2.5φ ($177 - 250\mu$m) grain size fractions were used. The 2 φ particles were dyed blue with clothing dye to aid in visualization. The 2.5 φ particles were undyed. The angles of repose for particles of the two grain-size fractions were measured in two types of slumping experiments yielding 34 ± 1 for the 2 φ particles and 35 ± 1 for the 2.5 φ particles. The 2.5 φ particles were poured onto the plane before each experiment to provide an erodible surface. The procedure was such that the thickness of the erodible layer would be h_{stop} of [3, 16]. The 2 φ particles were then released on this surface from a 10.5-cm diameter cylindrical container. The mass of particles released from the cylindrical container was 425 ± 0.9 g. The propagation of the sand was measured by videotaping while a horizontal grid was projected onto the plane to aid in visualization. Video frames were then grabbed with a digital frame grabber, and the sand propagation was measured directly from the frames by measuring the lateral spreading, as well as the advance of the head and tail of the flowing mass. Because of the difficulty in ascertaining the edge of the flow during time steps when the material was thinly spread, and because of geometrical distortions, the error in the measurements of positions of the flow is estimated to range from $1- \sim 2.5$ cm. The sand was allowed to flow off the end of the inclined plane into a collection bin. Because of the difference in particle size between the erodible bed and the flowing particles, we were able to separate the two fractions by sieving the collected material, and check the separation by ensuring that the colors of sand grains in the two sieved fractions were consistent with the initial colors. Using this technique, we were almost always able to ensure that $< 1\%$ of the blue, 2 φ particles were "lost" due to experimental error in each experiment. It was possible to determine an erosion gradient for the experiments by starting separate runs for every slope angle, at different positions on the inclined plane. In this way, particles were collected after flowing different distances down the plane. Using the erosion gradient and flow speed data, we could estimate erosion rate.

A typical experiment proceeded as follows (Fig. 1b-d). The videocamera was started and the operator

5

then filled the cylindrical container with sand as the base was placed flush to the test plane. The container was removed with a smooth motion to avoid undue disturbance of the particles. The test mass then began propagation downslope, although the tail remained stationary throughout an experimental run. The sand grains spread laterally as well as downstream, so that the mass rapidly attained a teardrop shape. As the widest part of the teardrop crossed the downstream edge of the plane, the outline of the flowing material attained the form of an inverted, elongated horseshoe. This form remained stable throughout the rest of each experiment, and changed only in becoming less blue with time as the 2 φ particles flowed off the edge. The only exception to this geometry was in experiments at angles within and less than the basal friction angle, in which case the mass was arrested on the upper test section when the experiment was initiated sufficiently high on the test slope.

3.2   Block and Ash Flows, Colima volcano

At Colima volcano, a dome of volume 2.2×10^5 collapsed to form a flow of volume 1×10^6 m^3 on 17 April 1991 during an eruption that lasted six hours overall (all volumes are reduced to equivalent deposit volume assuming dome density of 2500 and deposit density of 1500 kg/m^3.) In 1998-9 numerous eruptions resulted in block and ash flows of volume 2.4×10^6 m^3 [17, 18]. On 20 November 1998, a dome had grown in the summit crater to volume 6.5×10^5 m^3. A major eruption on 26 November 1998 resulted in the largest flow down the El Cordoban West gully reaching 4.5 km. Total volume of flow deposits in El Cordoban West gully is 8×10^5 m^3. Before this eruption, a lava flow with total volume $\sim 3 \times 10^5$ m^3 had extended about 400 m in the direction of the El Cordoban gullies. On 10 December a flow was observed propagating mostly down the El Cordoban East and La Lumbre gullies. No later activity was observed in the El Cordoban East gully. Total volume of deposits in the El Cordoban East and La Lumbre gullies is 8.1×10^5 m^3. Another major eruption on 17 July 1999 resulted in a deposit of volume 7.9×10^5 m^3 in the San Antonio-Montegrande gully. The estimated size of the crater created during this event is approximately the same as the deposit volume.

Although the estimates of initial volumes and deposit volumes for the eruptions at Colima volcano (as indeed they are for any eruption) are susceptible to a great deal of questioning, it might be reasonable to consider that initial collapse volumes of $2 - 10 \times 10^5$ m^3 can result in deposit volumes of $8 - 10 \times 10^5$ m^3. We thus did a number of model runs on the topography of Colima volcano, using an initial volume of $\sim 3 \times 10^5$ m^3 to test the value of the erosion parameter β necessary to obtain a deposit volume of 8×10^5 m^3.

4   Discussion and Conclusions

Because it is not possible to distinguish bed particles from flowing particles in the model, the results of comparison of model output with laboratory data can be summarized by comparing both the mass of

6

particles transported off the end of the test slope, as well as the mass left on the test slope as a function of distance flowed (Fig. 2). The difference between these is the net deposition or erosion. As slope angle and distance of the starting mass from the end of the slope (transport distance) increased, the total mass of particles that were transported off the slope increased in both data and model. The values for the empirical erosion parameters (Eqn. 4, 5) used in the model runs was $\beta = 0.1$ and $n = 1/2$. The results suggest that the model is able to reproduce erosion conditions reasonably well over a range of slope angle and slope length conditions.

There are large uncertainties inherent in any estimate of flow deposit volume, for virtually any flow. This is the result of a paucity of information about the pre-existing surface. Nevertheless, the data are consistent with block and ash flows at Colima volcano sometimes being able to erode a small multiple of their original volume (Fig. 3). Using reasonable initial and final volumes, we found that a value for the erosion parameter, $\beta \sim 0.15$, fits our example test case. It is perhaps encouraging that the value of the erosion parameter is of the same order of magnitude in experiments and in a typical example of a natural flow. Erosion affects runout (Fig. 4). Because of the interaction between the flowing mass and variable basal topography, mean flow speed, for example, is a complex function of erosion coefficient. Thus erosion should be considered in any hazard model of volcanic granular flow.

There are a number of shortcomings in the current approach. The erosion model is based on an assumed dynamical similarity between erosion in clear-water flows and granular flows. The value for the erosion parameter is determined empirically and we have developed no *a priori* manner in which to find it. Field data for testing of the model are sparse and subject to great uncertainties. Finally, we have only discussed a methodology for incorporating erosion into a granular flow model, we have not explored the effects of erosion on flow dynamics or on estimation of inundation areas and runout distances, so important to hazards analysis.

References

[1] E. S. Calder, R. Stephen J. Sparks, and M. C. Gardeweg. Erosion, transport and segregation of pumice and lithic clasts in pyroclastic flows inferred from ignimbrite at Lascar Volcano, Chile. *Journal of Volcanology and Geothermal Research*, 104(1-4):201–235, 2000.

[2] P.D. Cole, E.S. Calder, R.S.J. Sparks, A.B. Clarke, T.H. Druitt, S.R. Young, R.A. Herd, C.L. Harford, and G.E. Norton. Deposits from dome-collapse and fountain-collapse pyroclastic flows at Soufriere

7

Hills Volcano, montserrat. In T.H. Druitt and B.P. Kokelaar, editors, *The Eruption of Soufriere Hills Volcano, Montserrat, From 1995 to 1999*, volume 21 of *Memoirs*, pages 231–262. Geological Society, London, 2002.

[3] Adrian Daerr. Dynamical equilibrium of avalanches on a rough plane. *Physics of Fluids*, 13(7):2115–2124, 2001.

[4] T.H. Druitt. Pyroclastic density currents. In J.S. Gilbert and R.S.J. Sparks, editors, *The Physics of Explosive Volcanic Eruptions*, volume 145 of *Special Publications*, pages 145–182. Geological Society, London, 1998.

[5] Egashira S.,Honda N. and Itoh T., Experimental study on the entrainment of bed material into debris flow,*Physics and Chemistry of the Earth, Part C: Solar, Terrestrial & Planetary Science*, Volume 26, Issue 9, September 2001, Pages 645-650.

[6] Faeh Roland, Erosion-based Dambreak Simulation, Laboratory of Hydraulics, Hydrology and Glaciology of the Swiss Federal Institute of Technology, Report, 1996

[7] A. Freundt and M. Bursik. Pyroclastic flow transport mechanisms. In A. Freundt and M. Rosi, editors, *From Magma to Tephra: Modelling Physical Processes of Explosive Volcanism*, volume 4 of *Developments in Volcanology*, pages 151–222. Elsevier, Amsterdam, 1998.

[8] Fraccarollo L., and Capart H., Riemann wave description of erosional dam-break flows, J Fluid Mech, 461, 183-228, 2002

[9] Iverson, R.M., The physics of debris flow,*Rev. Geophys*, 35 pp245-296, 1997a.

[10] Iverson R.M., and Denlinger R.P., Flow of variably fluidized granular masses across three-dimensional terrain. 1 Coulomb mixture theory, *Journal of Geophysical Research*, vol 106 No B1, pp537-552, jan 10, 2001.

[11] Khakhar D.V., Orpe A.V., Andersen P. and Ottino J.M., Surface flow of granular materials: model and experiments in heap formation, *J. Fluid Mech.*, vol 441, 2001, pp 255-264.

[12] F. Legros. The mobility of long-runout landslides. *Engineering Geology*, 63:301–331, 2002.

[13] Ng, F., Mathematical Modeling of Subglacial Drainage and Erosion, Ph.D. Thesis, St. Catherine's College, Oxford, 1998.

[14] Kovacs A., and Parker G., A new vectorial bedload formulation and its applications to the time evolution of straight river channels,*J Fluid Mech*, 1994, 267, 153-183.

8

85

[15] A.K. Patra, A.C. Bauer, C. Nichita, E.B. Pitman, M.F. Sheridan, M. Bursik, B. Rupp, A. Webb, L. Namikawa, and C. Renschler. Parallel adaptive numerical simulation of dry avalanches over natural terrain. *J. Volcanic and Geothermal Research*. in press.

[16] Olivier Pouliquen and Yoël Forterre. Friction law for dense granular flows: application to the motion of a mass down a rough inclined plane. *Journal of Fluid Mechanics*, 453:133–151, 2002.

[17] R. Saucedo, J.-L. Macias, M. Bursik, J. Mora, J. Gavilanes, and A. Cortes. Emplacement of pyroclastic flows during the 1998-1999 eruption of Volcàn de Colima, México. *Journal of Volcanology and Geothermal Research*, 117:129–153, 2002.

[18] R. Saucedo, J.-L. Macias, and M. Bursik. Pyroclastic flow deposits of the 1991 eruption of Volcán de Colima, Mexico. *Bulletin of Volcanology*, 2003. Online 9 October 2003.

[19] Savage S.B., and Hutter K., The motion of a finite mass of granular material down a rough incline, *J Fluid Mech*, 199, pp177-215, 1989.

[20] K. M. Scott, J. W. Vallance, and P. T. Pringle. Sedimentology, behavior, and hazards of debris flows at Mount Rainier, Washington. *U. S. Geological Survey Professional Paper*, 1547:1–56, 1995.

[21] Takahashi, T. and S.F. Kuang, 1986 Formation of debris flows on varied slope bed.*Annuals, Disas. Prev. Res. Inst., Kyoto Univ.* 29B-2:343-359(in Japanese).

[22] T. Ui, N. Matsuwo, M. Sumita, and A. Fujinawa. Generation of block and ash flows during the 1990-1995 eruption of Unzen Volcano, Japan. *Journal of Volcanology and Geothermal Research*, 89:123–137, 1999.

[23] B. Voight, J. C. Komorowski, G. E. Norton, A. B. Belousov, M. Belousova, G. Boudon, P. W. Francis, W. Franz, P. Heinrich, R. Steve J. Sparks, and S. R. Young. The 26 December (Boxing Day) 1997 sector collapse and debris avalanche at Soufriere Hills Volcano, Montserrat. In T.H. Druitt and B.P. Kokelaar, editors, *The Eruption of Soufriere Hills Volcano, Montserrat, From 1995 to 1999*, volume 21 of *Memoirs*, pages 363–407. Geological Society, London, 2002.

9

Table 1: Erosional grain flow experiments. For all experiments, 2 and 2.5φ sand particles were used.

Experiment number	Angle	Mass (g)	Release point‡ (cm)	Mass 2.5φ eroded (g)	Mass 2φ trans'd (g)	Total mass in bin	Mass 2φ lost (g)
eabgf294a	29.4	425.13	1	0	0	0	0
eabgf294b	29.4	425.20	1	0	0	0	0
eabgf294c	29.4	425.52	17.5	0	0	0	0
eabgf294d	29.4	425.10	20	0	0	0	0
eabgf294e	29.4	425.24	41.5	0	0	0	0
eabgf294f	29.4	425.25	40.5	0	0	0	0
eabgf294g	29.4	425.21	67.5	3.78	142.85	146.63	7.14
eabgf294h	29.4	425.36	67.5	6.73	154.76	161.49	4.59
eabgf322a	32.2	425.5	1.5	0	0	0	0
eabgf322b	32.2	425.11	.5	0	0	0	0
eabgf322c	32.2	425.02	19.5	2.38	19.05	21.43	5.36
eabgf322d	32.2	425.19	19	5.5	42.49	48	4.23
eabgf322e	32.2	425.45	46	22.48	210.16	232.64	4.59
eabgf322f	32.2	425.07	44	25.78	195.62	3.28	
eabgf322g	32.2	425.17	69	20.47	368.45	388.97	5.30
eabgf322h	32.2	425.17	70	16.43	365.19	371.62	5.94
eabgf344a	34.4	425.44	1	45.77	187.82	233.59	5.52
eabgf344b	34.4	425.13	2	37.62	188.89	226.51	5.09
eabgf344c	34.4	425.55	18	46.93	227.58	274.51	4.79
eabgf344d	34.4	425.33	18.5	36.3	242.10	278.4	5.65
eabgf344e	34.4	425.06	44.5	34.18	317.36	351.54	2.24
eabgf344f	34.4	425.49	44.5	30.08	318.42	348.5	5.70
eabgf344g	34.4	425.75	68	17.12	390.93	408.05	3.24
eabgf344h	34.4	425.13	68	13.04	374.92	387.96	5.86
eabgf365a	36.5	425.22	2	131.85	326.66	458.51	3.34
eabgf365b	36.5	425.68	2	128.18	334.62	462.62	2.07
eabgf365c	36.5	425.29	19.5	95.9	362.05	457.95	2.88
eabgf365d	36.5	425.51	20	105.32	361.31	466.63	1.37
eabgf365e	36.5	425.29	38	74.96	377.43	452.39	3.62
eabgf365g	36.5	425.54	40	53.97	389.73	443.7	4.8
eabgf365h	36.5	425.42	68	32.4	404.53	409.53	5.0
eabgf365i	36.5	425.82	61	28.71	406.4	435.11	4.33

‡Release point is the distance of the top of the test cylinder from the upper edge of the slope.

10
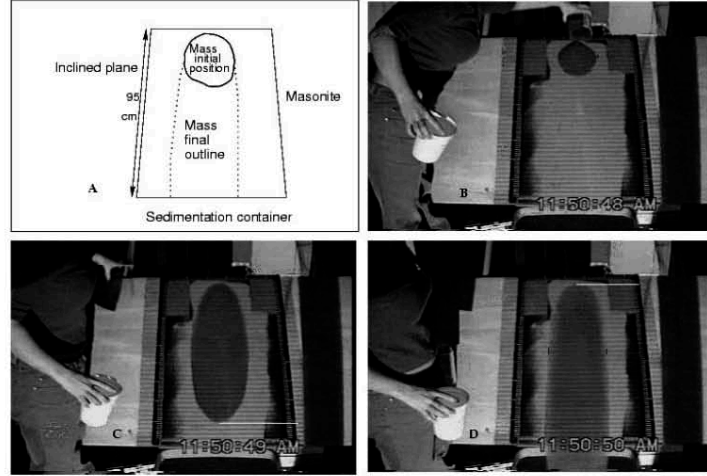
5 Figures

Figure 1: Experimental setup and example runs. a) Schematic diagram traced from image showing positions of masonite plane and sand masses. Lighter area on the masonite plane is outline of 2.5φ undyed particles. Angle of plane was measured with a digital construction level. b) Starting of experiment at 36.5(eabgf3656a) with mass of 425.22 g. Image taken 0.2 s after start of experiment. c) Moving 2φ mass with teardrop shape. Image taken 1.0 s after start of experiment. d) Final outline of mass on plane, with mass flowing off edge of plane into sedimentation container. This outline remained with time although fraction of dyed 2φ particles within it decreased to the end of the experiment. Image taken 2.2 s after start of experiment.

11

88
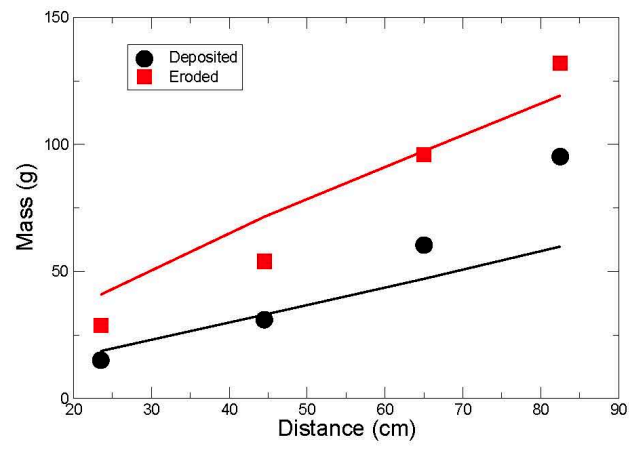
Figure 2: Results of comparison of the erosional model with experimental data. These results are for a slope angle of 36.5 deg, $\beta = 0.1$ and $n = 1/2$.

12
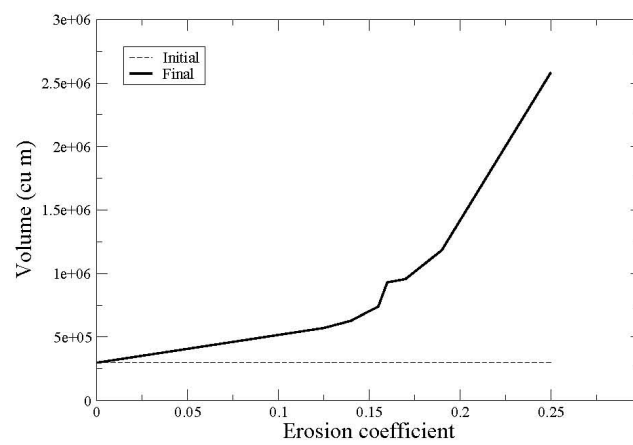
Figure 3: Initial and final block and ash flow volume as a function of erosion coefficient, β for flow down the topography of Colima volcano. At a value of $\beta \sim 0.15$, final volume is similar to that of our example test case.

13
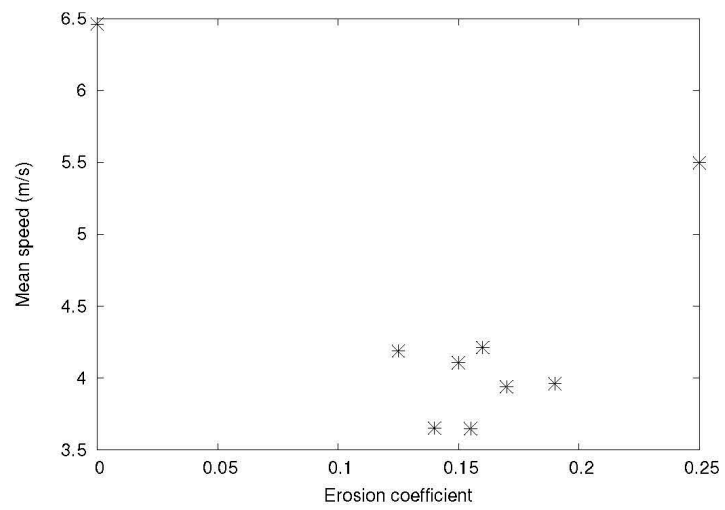
Figure 4: Time-average flow speed for flows shown in Figure 3. Flow speed is a complex function of β.

14

Appendix D

Rough Inclined Plane Erosion Data

Angle 29.4

Erosion Rate

Averaged Experiment Data	2.5phi eroded off (g)	Total Length (cm)	Ave. Mean Width (cm)	Distance down from hashmarks (cm)
Top Release: a,b	0.00	0.00	18.05	5.75
1/4 Down Release: c,d	0.00	43.75	18.29	22.50
3/4 Down Release: e,f	0.00	43.25	15.33	45.75
Bottom Release: g,h	5.26	24.50	18.21	72.25

Eroded Section	Time (s)	Ave. Mean Width (cm)	Erosion Rate (cm/s)	Center of Section (cm)
Top Section (a,b - c,d)	0.30	18.17	0.00	14.13
Middle Section (c,d - e,f)	0.36	16.81	0.00	34.13
Bottom Section (e,f - g,h)	0.43	16.77	0.51	59.00

Experiment Data

Experiment A: Released near the top
Position of the middle of the cylinder from the top of the plane (cm): 5.75

Frame	Width at bottom (cm)
bgf294a080	10
bgf294a088	16
bgf294a096	22
bgf294a104	20.5
bgf294a114	20
SUM:	88.5

*Measurements of final deposit and eroded material:
- Total Length (cm): 38
- Weight of 2.5 phi particles in bin (g): 0
- Weight of 2 phi particles in bin (g): 0
- Weight of 2 phi particles on inclined plane (g): 425.13
- Weight of 2 phi particles lost (g): 0

Experiment B: Released near the top
Position of the middle of the cylinder from the top of the plane (cm): 5.75

Frame	Width at bottom (cm)
bgf294a080	10
bgf294a088	19.5
bgf294a096	21
bgf294a104	21.5
bgf294a114	20
SUM:	92

*Measurements of final deposit and eroded material:
- Total Length (cm): 42
- Weight of 2.5 phi particles in bin (g): 0
- Weight of 2 phi particles in bin (g): 0
- Weight of 2 phi particles on inclined plane (g): 425.2
- Weight of 2 phi particles lost (g): 0

Experiment C: Released 1/4 the way down
Position of the middle of the cylinder from the top of the plane (cm): 21.75

Frame	Width at bottom (cm)
bgf294c123	11
bgf294c131	17
bgf294c136	20.5
bgf294c141	20
bgf294c146	20
bgf294c157	19
SUM:	107.5

*Measurements of final deposit and eroded material:
- Total Length (cm): 42.5
- Weight of 2.5 phi particles in bin (g): 0
- Weight of 2 phi particles in bin (g): 0
- Weight of 2 phi particles on inclined plane (g): 425.52
- Weight of 2 phi particles lost (g): 0

Experiment D: Released 1/4 the way down
Position of the middle of the cylinder from the top of the plane (cm): 23.25

Frame	Width at bottom (cm)
bgf294d026	10
bgf294d034	16
bgf294d039	21.5
bgf294d044	21.5
bgf294d049	21.5

94

bgf294d054	21.5
SUM:	112

*Measurements of final deposit and eroded material:
- Total Length (cm): 45
- Weight of 2.5 phi particles in bin (g): 0
- Weight of 2 phi particles in bin (g): 0
- Weight of 2 phi particles on inclined plane (g): 425.1
- Weight of 2 phi particles lost (g): 0

Experiment E: Released 3/4 the way down
Position of the middle of the cylinder from the top of the plane (cm): 46.25

Frame	Width at bottom (cm)
bgf294e163	10
bgf294e169	13
bgf294e175	17
bgf294e181	17.5
bgf294e188	17
bgf294e198	16.5
SUM:	91

*Measurements of final deposit and eroded material:
- Total Length (cm): 44
- Weight of 2.5 phi particles in bin (g): 0
- Weight of 2 phi particles in bin (g): 0
- Weight of 2 phi particles on inclined plane (g): 425.24
- Weight of 2 phi particles lost (g): 0

Experiment F: Released 3/4 the way down
Position of the middle of the cylinder from the top of the plane (cm): 45.25

Frame	Width at bottom (cm)
bgf294f096	10.5
bgf294f102	13
bgf294f108	17.5
bgf294f114	18
bgf294f120	17.5
bgf294f130	16.5
SUM:	93

*Measurements of final deposit and eroded material:
- Total Length (cm): 42.5

- Weight of 2.5 phi particles in bin (g): 0
- Weight of 2 phi particles in bin (g): 0
- Weight of 2 phi particles on inclined plane (g): 425.25
- Weight of 2 phi particles lost (g): 0

Experiment G: Released near the bottom
Position of the middle of the cylinder from the top of the plane (cm): 72.25

Frame	Width at bottom (cm)
bgf294g102	9.5
bgf294g108	14
bgf294g112	19.5
bgf294g118	22
bgf294g148	22
bgf294g182	22
SUM:	109

*Measurements of final deposit and eroded material:
- Total Length (cm): 24.5
- Weight of 2.5 phi particles in bin (g): 3.78
- Weight of 2 phi particles in bin (g): 142.85
- Weight of 2 phi particles on inclined plane (g): 275.22
- Weight of 2 phi particles lost (g): 7.14

Experiment H: Released near the bottom
Position of the middle of the cylinder from the top of the plane (cm): 72.25

Frame	Width at bottom (cm)
bgf294h180	9.5
bgf294h186	14
bgf294h190	20
bgf294h196	22
bgf294h225	22
bgf294h255	22
SUM:	109.5

*Measurements of final deposit and eroded material:
- Total Length (cm): 24.5
- Weight of 2.5 phi particles in bin (g): 6.73
- Weight of 2 phi particles in bin (g): 154.76
- Weight of 2 phi particles on inclined plane (g): 266.01
- Weight of 2 phi particles lost (g): 4.59

Table D.1: Erosion data collected on avalanches initiated at angle 29.4

Angle 32.2

Erosion Rate

Averaged Experiment Data	2.5phi eroded off (g)	Total Length (cm)	Ave. Mean Width (cm)	Distance down from hashmarks (cm)
Top Release: a,b	0.00	89.50	16.97	5.88
1/4 Down Release: c,d	3.94	72.25	18.04	24.25
3/4 Down Release: e,f	24.13	46.50	18.71	50.25
Bottom Release: g,h	18.45	22.00	17.75	74.75

Eroded Section	Time (s)	Ave. Mean Width (cm)	Erosion Rate (cm/s)	Center of Section (cm)
Top Section (a,b - c,d)	0.32	17.50	0.49	15.06
Middle Section (c,d - e,f)	0.38	18.37	2.01	37.25
Bottom Section (e,f - g,h)	0.4	18.23	0.54	62.50

Experiment Data

Experiment A: Released near the top
Position of the middle of the cylinder from the top of the plane (cm): 6.25

Frame	Width at bottom (cm)
bgf322a228	10
bgf322a236	18
bgf322a244	23
bgf322a270	22
bgf322a320	20.25
bgf322a370	17
bgf322a420	14
bgf322a470	12
SUM:	136.25

*Measurements of final deposit and eroded material:
- Total Length (cm): 90
- Weight of 2.5 phi particles in bin (g): 0
- Weight of 2 phi particles in bin (g): 0
- Weight of 2 phi particles on inclined plane (g): 425.5
- Weight of 2 phi particles lost (g): 0

Experiment B: Released near the top
Position of the middle of the cylinder from the top of the plane (cm): 5.5

Frame	Width at bottom (cm)
bgf322b022	10.5
bgf322b030	16.5
bgf322b038	23
bgf322b065	21.75
bgf322b090	20
bgf322b140	17
bgf322b190	13.5
bgf322n240	13
SUM:	135.25

*Measurements of final deposit and eroded material:
- Total Length (cm): 89
- Weight of 2.5 phi particles in bin (g): 0
- Weight of 2 phi particles in bin (g): 0
- Weight of 2 phi particles on inclined plane (g): 425.11
- Weight of 2 phi particles lost (g): 0

Experiment C: Released 1/4 the way down
Position of the middle of the cylinder from the top of the plane (cm): 24.25

Frame	Width at bottom (cm)
bgf322c115	10.5
bgf322c125	20.5
bgf322c135	23.25
bgf322c168	21
bgf322c200	18
bgf322c250	18.5
bgf322c300	18
SUM:	129.75

*Measurements of final deposit and eroded material:
- Total Length (cm): 72
- Weight of 2.5 phi particles in bin (g): 2.38
- Weight of 2 phi particles in bin (g): 19.05
- Weight of 2 phi particles on inclined plane (g): 400.61
- Weight of 2 phi particles lost (g): 5.36

Experiment D: Released 1/4 the way down
Position of the middle of the cylinder from the top of the plane (cm): 24.25

Frame	Width at bottom (cm)
bgf322d155	11
bgf322d165	20.25
bgf322d175	22
bgf322d200	18.5
bgf322d225	17
bgf322d275	17
bgf322d325	17
SUM:	122.75

*Measurements of final deposit and eroded material:
- Total Length (cm): 72.5
- Weight of 2.5 phi particles in bin (g): 5.5
- Weight of 2 phi particles in bin (g): 42.49
- Weight of 2 phi particles on inclined plane (g): 378.47
- Weight of 2 phi particles lost (g): 4.23

Experiment E: Released 3/4 the way down
Position of the middle of the cylinder from the top of the plane (cm): 51.25

Frame	Width at bottom (cm)
bgf322e517	10.25
bgf322e527	19.5
bgf322e532	19
bgf322e537	20.5
bgf322e601	22.5
bgf322e665	22.5
SUM:	114.25

*Measurements of final deposit and eroded material:
- Total Length (cm): 45.5
- Weight of 2.5 phi particles in bin (g): 22.48
- Weight of 2 phi particles in bin (g): 210.16
- Weight of 2 phi particles on inclined plane (g): 210.7
- Weight of 2 phi particles lost (g): 4.59

Experiment F: Released 3/4 the way down
Position of the middle of the cylinder from the top of the plane (cm): 49.25

Frame	Width at bottom (cm)
bgf322f076	10.25
bgf322f086	17
bgf322f091	20

bgf322f096	20
bgf322f156	21.5
bgf322f215	21.5
SUM:	110.25

*Measurements of final deposit and eroded material:
- Total Length (cm): 47.5
- Weight of 2.5 phi particles in bin (g): 25.78
- Weight of 2 phi particles in bin (g): 195.62
- Weight of 2 phi particles on inclined plane (g): 226.17
- Weight of 2 phi particles lost (g): 3.28

Experiment G: Released near the bottom
Position of the middle of the cylinder from the top of the plane (cm): 74.25

Frame	Width at bottom (cm)
bgf322g035	9
bgf322g040	14
bgf322g045	21.5
bgf322g094	21
bgf322g144	21.5
SUM:	87

*Measurements of final deposit and eroded material:
- Total Length (cm): 22.5
- Weight of 2.5 phi particles in bin (g): 20.47
- Weight of 2 phi particles in bin (g): 368.45
- Weight of 2 phi particles on inclined plane (g): 51.42
- Weight of 2 phi particles lost (g): 5.3

Experiment H: Released near the bottom
Position of the middle of the cylinder from the top of the plane (cm): 75.25

Frame	Width at bottom (cm)
bgf322h082	9
bgf322h087	14.5
bgf322h092	22.5
bgf322h137	22.5
bgf322h187	22
SUM:	90.5

*Measurements of final deposit and eroded material:
- Total Length (cm): 21.5

- Weight of 2.5 phi particles in bin (g): 16.43
- Weight of 2 phi particles in bin (g): 365.19
- Weight of 2 phi particles on inclined plane (g): 54.76
- Weight of 2 phi particles lost (g): 5.84

Table D.2: Erosion data collected on avalanches initiated at angle 32.2°.

Angle 34.4

Erosion Rate

Averaged Experiment Data	2.5phi eroded off (g)	Total Length (cm)	Ave. Mean Width (cm)	Distance down from hashmarks (cm)
Top Release: a,b	41.70	90.00	20.56	6.00
1/4 Down Release: c,d	41.77	73.25	19.64	23.38
3/4 Down Release: e,f	32.13	47.00	20.77	49.50
Bottom Release: g,h	15.08	23.50	17.75	73.00

Eroded Section	Time (s)	Ave. Mean Width (cm)	Erosion Rate (cm/s)	Center of Section (cm)
Top Section (a,b - c,d)	0.30	20.10	0.01	14.69
Middle Section (c,d - e,f)	0.38	20.21	0.87	36.44
Bottom Section (e,f - g,h)	0.32	19.26	1.92	61.25

Experiment Data
Experiment A: Released near the top
Position of the middle of the cylinder from the top of the plane (cm): 6

Frame	Width at bottom (cm)
bgf344a265	11
bgf344a275	20.5
bgf344a285	21.5
bgf344a295	22.5
bgf344a325	20
bgf344a350	22
bgf344a450	22.5
bgf344a550	22.5
SUM:	162.5

*Measurements of final deposit and eroded material:

- Total Length (cm): 90.5
- Weight of 2.5 phi particles in bin (g): 45.77
- Weight of 2 phi particles in bin (g): 187.82
- Weight of 2 phi particles on inclined plane (g): 232.1
- Weight of 2 phi particles lost (g): 5.52

Experiment B: Released near the top
Position of the middle of the cylinder from the top of the plane (cm): 6

Frame	Width at bottom (cm)
bgf344b169	10.5
bgf344b179	21
bgf344b189	22.5
bgf344b199	23.5
bgf344b230	21
bgf344b260	22.5
bgf344b360	22.5
bgf344b460	23
SUM:	166.5

*Measurements of final deposit and eroded material:
- Total Length (cm): 89.5
- Weight of 2.5 phi particles in bin (g): 37.62
- Weight of 2 phi particles in bin (g): 188.89
- Weight of 2 phi particles on inclined plane (g): 231.15
- Weight of 2 phi particles lost (g): 5.09

Experiment C: Released 1/4 the way down
Position of the middle of the cylinder from the top of the plane (cm): 23.25

Frame	Width at bottom (cm)
bgf344c159	10
bgf344c164	13
bgf344c169	19.5
bgf344c179	24
bgf344c211	23
bgf344c311	24
bgf344c411	23.5
SUM:	137

*Measurements of final deposit and eroded material:
- Total Length (cm): 73.5
- Weight of 2.5 phi particles in bin (g): 46.93

- Weight of 2 phi particles in bin (g): 227.58
- Weight of 2 phi particles on inclined plane (g): 193.18
- Weight of 2 phi particles lost (g): 4.79

Experiment D: Released 1/4 the way down
Position of the middle of the cylinder from the top of the plane (cm): 23.5

Frame	Width at bottom (cm)
bgf344d352	10.5
bgf344d357	13
bgf344d362	20
bgf344d372	23.5
bgf344d400	23
bgf344d495	24
bgf344d595	24
SUM:	138

*Measurements of final deposit and eroded material:
- Total Length (cm): 73
- Weight of 2.5 phi particles in bin (g): 36.6
- Weight of 2 phi particles in bin (g): 242.1
- Weight of 2 phi particles on inclined plane (g): 177.58
- Weight of 2 phi particles lost (g): 5.65

Experiment E: Released 3/4 the way down
Position of the middle of the cylinder from the top of the plane (cm): 49.5

Frame	Width at bottom (cm)
bgf344e052	10
bgf344e057	14.25
bgf344e062	21
bgf344e067	23
bgf344e077	26
bgf344e125	26
bgf344e225	26
SUM:	146.25

*Measurements of final deposit and eroded material:

- Total Length (cm): 47
- Weight of 2.5 phi particles in bin (g): 34.18
- Weight of 2 phi particles in bin (g): 317.36
- Weight of 2 phi particles on inclined plane (g): 105.46
- Weight of 2 phi particles lost (g): 2.24

Experiment F: Released 3/4 the way down

Position of the middle of the cylinder from the top of the plane (cm): 49.5

Frame	Width at bottom (cm)
bgf344f073	10
bgf344f080	15.5
bgf344f085	21
bgf344f090	22.5
bgf344f100	24.5
bgf344f155	25.5
bgf344f255	25.5
SUM:	144.5

*Measurements of final deposit and eroded material:
- Total Length (cm): 47
- Weight of 2.5 phi particles in bin (g): 30.08
- Weight of 2 phi particles in bin (g): 318.42
- Weight of 2 phi particles on inclined plane (g): 101.37
- Weight of 2 phi particles lost (g): 5.7

Experiment G: Released near the bottom
Position of the middle of the cylinder from the top of the plane (cm): 72.75

Frame	Width at bottom (cm)
bgf344g062	9.5
bgf344g067	14
bgf344g072	21
bgf344g131	22
bgf344g190	22
SUM:	88.5

*Measurements of final deposit and eroded material:
- Total Length (cm): 23.5
- Weight of 2.5 phi particles in bin (g): 17.12
- Weight of 2 phi particles in bin (g): 390.93
- Weight of 2 phi particles on inclined plane (g): 31.58
- Weight of 2 phi particles lost (g): 3.24

Experiment H: Released near the bottom
Position of the middle of the cylinder from the top of the plane (cm): 73.25

Frame	Width at bottom (cm)
bgf344h148	9
bgf344h152	12.5
bgf344h157	21.5
bgf344h208	23
bgf344h260	23
SUM:	89

*Measurements of final deposit and eroded material:
- Total Length (cm): 23.5
- Weight of 2.5 phi particles in bin (g): 13.04
- Weight of 2 phi particles in bin (g): 374.92
- Weight of 2 phi particles on inclined plane (g): 44.35
- Weight of 2 phi particles lost (g): 5.86

Table D.3: Erosion data collected on avalanches initiated at angle 34.4°.

Angle 36.5

Erosion Rate

Averaged Experiment Data	2.5phi eroded off (g)	Total Length (cm)	Ave. Mean Width (cm)	Distance down from hashmarks (cm)
Top Release: a,b	130.02	89.50	22.02	6.25
1/4 Down Release: c,d	100.61	71.75	22.15	23.75
3/4 Down Release: e,f	64.47	52.50	21.22	42.88
Bottom Release: g,h	30.56	30.50	18.32	65.25

Eroded Section	Time (s)	Ave. Mean Width (cm)	Erosion Rate (cm/s)	Center of Section (cm)
Top Section (a,b - c,d)	0.23	22.09	4.02	15.00
Middle Section (c,d - e,f)	0.26	21.68	4.45	33.31
Bottom Section (e,f - g,h)	0.31	19.77	3.84	54.06

Experiment Data

Experiment A: Released near the top
Position of the middle of the cylinder from the top of the plane (cm): 6.25

Frame	Width at bottom (cm)
bgf365a330	10

Frame	Width at bottom (cm)
bgf365a336	17.5
bgf365a342	25
bgf365a348	23.5
bgf365a354	23.5
bgf365a360	22
bgf365a366	22.5
bgf365a396	25.5
bgf365a470	24
bgf365a570	24.5
bgf365a670	25
SUM:	243

*Measurements of final deposit and eroded material:
- Total Length (cm): 89.5
- Weight of 2.5 phi particles in bin (g): 131.85
- Weight of 2 phi particles in bin (g): 326.66
- Weight of 2 phi particles on inclined plane (g): 95.22
- Weight of 2 phi particles lost (g): 3.34

Experiment B: Released near the top
Position of the middle of the cylinder from the top of the plane (cm): 6.25

Frame	Width at bottom (cm)
bgf365b321	11
bgf365b327	17
bgf365b333	23.5
bgf365b339	22.5
bgf365b345	21
bgf365b351	22
bgf365b357	23
bgf365b387	26
bgf365b450	25
bgf365b550	25.5
bgf365b650	25
SUM:	241.5

*Measurements of final deposit and eroded material:
- Total Length (cm): 89.5
- Weight of 2.5 phi particles in bin (g): 128.18
- Weight of 2 phi particles in bin (g): 334.62
- Weight of 2 phi particles on inclined plane (g): 88.99
- Weight of 2 phi particles lost (g): 2.07

Experiment C: Released 1/4 the way down
Position of the middle of the cylinder from the top of the plane (cm): 23.75

Frame	Width at bottom (cm)
bgf365c640	11
bgf365c646	14.5
bgf365c652	23
bgf365c658	21.5
bgf365c664	23
bgf365c670	25
bgf365c700	26
bgf365c745	25
bgf365c845	25.5
bgf365c945	26
SUM:	220.5

*Measurements of final deposit and eroded material:
- Total Length (cm): 72
- Weight of 2.5 phi particles in bin (g): 95.9
- Weight of 2 phi particles in bin (g): 362.05
- Weight of 2 phi particles on inclined plane (g): 60.36
- Weight of 2 phi particles lost (g): 2.88

Experiment D: Released 1/4 the way down
Position of the middle of the cylinder from the top of the plane (cm): 23.75

Frame	Width at bottom (cm)
bgf365d437	11
bgf365d443	16
bgf365d449	23.5
bgf365d455	22.5
bgf365d461	22.5
bgf365d467	25.5
bgf365d500	25
bgf365d550	25.5
bgf365d650	26
bgf365d750	25
SUM:	222.5

*Measurements of final deposit and eroded material:
- Total Length (cm): 71.5
- Weight of 2.5 phi particles in bin (g): 105.32
- Weight of 2 phi particles in bin (g): 361.31
- Weight of 2 phi particles on inclined plane (g): 62.83
- Weight of 2 phi particles lost (g): 1.37

Experiment E: Released 3/4 the way down
Position of the middle of the cylinder from the top of the plane (cm): 41

Frame	Width at bottom (cm)
bgf365e046	9.5
bgf365e052	14.5
bgf365e058	20.5
bgf365e064	23.5
bgf365e070	26.5
bgf365e100	24.5
bgf365e160	24.5
bgf365e260	24
SUM:	167.5

*Measurements of final deposit and eroded material:
- Total Length (cm): 53.5
- Weight of 2.5 phi particles in bin (g): 74.96
- Weight of 2 phi particles in bin (g): 377.43
- Weight of 2 phi particles on inclined plane (g): 44.24
- Weight of 2 phi particles lost (g): 3.62

Experiment G: Released 3/4 the way down
Position of the middle of the cylinder from the top of the plane (cm): 44.75

Frame	Width at bottom (cm)
bgf365g155	10
bgf365g161	17
bgf365g167	21.5
bgf365g173	25
bgf365g179	26
bgf365g209	24.5
bgf365g309	24
bgf365g409	24
SUM:	172

*Measurements of final deposit and eroded material:
- Total Length (cm): 51.5
- Weight of 2.5 phi particles in bin (g): 53.97
- Weight of 2 phi particles in bin (g): 389.73
- Weight of 2 phi particles on inclined plane (g): 31.01
- Weight of 2 phi particles lost (g): 4.8

Experiment H: Released near the bottom
Position of the middle of the cylinder from the top of the plane (cm): 64.25

Frame	Width at

	bottom (cm)
bgf365h214	9.5
bgf365h218	11
bgf365h222	19.5
bgf365h226	24.5
bgf365h232	23
bgf365h284	21
bgf365h234	21.5
SUM:	130

*Measurements of final deposit and eroded material:
- Total Length (cm): 30.5
- Weight of 2.5 phi particles in bin (g): 32.4
- Weight of 2 phi particles in bin (g): 404.53
- Weight of 2 phi particles on inclined plane (g): 15.89
- Weight of 2 phi particles lost (g): 5

Experiment I: Released near the bottom
Position of the middle of the cylinder from the top of the plane (cm): 66.25

Frame	Width at
	bottom (cm)
bgf365i244	9.5
bgf365i248	11
bgf365i252	17.5
bgf365i256	23.5
bgf365i260	23
bgf365i336	21.5
bgf365i436	20.5
SUM:	126.5

*Measurements of final deposit and eroded material:
- Total Length (cm): 30.5
- Weight of 2.5 phi particles in bin (g): 28.71
- Weight of 2 phi particles in bin (g): 406.4
- Weight of 2 phi particles on inclined plane (g): 15.09
- Weight of 2 phi particles lost (g): 4.33

Table D.4: Erosion data collected on avalanches initiated at angle 36.5°.

Appendix E

MotionPro System Specification Sheet

MotionPro High-Speed CMOS PCI Camera: www.redlake.com

Redlake's MotionPro high-speed CMOS PCI camera combines an advanced high-speed, mega-pixel resolution CMOS camera with the features you need for meaningful high-speed motion analysis on your PC. Designed as a peripheral for capturing high-speed digital images directly into the PC, the MotionPro system consists of a high-speed camera, full size single-slot PCI camera control and frame storage board (with up to 6 GB onboard memory), user interface, and easy-to-use analysis software. Up to four MotionPro systems can be operated in a single PC, providing multiple synchronous views of a high-speed event. Video capture using MotionPro cameras may be initiated via software or a wide variety of external triggers including optical, acoustic, electrical, and motion-controlled devices, as well as simple handheld switches. Flexible recording options offer several recording modes allowing the user to either use the memory as a circular buffer into which specified numbers of pre- and post-trigger frames may be recorded, or to divide the memory into a segmented buffer for multiple session operation. Motion analysis software completes the system functionality with many valuable features including angular, linear, velocity and rotational measurements as well as tracking multiple points over multiple frames. The MotionPro also has a lens calculator tool that computes lens selection, depth of field, magnification factor and motion blur for any setup.

P erformance Specifications

Sensor Array: Ten Channel 1280 x 1024 pixel CMOS Sensor.
Image Resolution: Up to 1280 x 1024. Pixel depth is 8 bits (mono), 24 bits (color).
Sensitivity:
-500 - up to 500 frames per second
-2000 - up to 2,000 frames per second
-10000 - up to 10,000 frames per second
Shutter: Global Electronic Shutter with exposure times from 2μ seconds to 1/frame rate in increments of 2μ seconds.
Lens Mount: Standard C-mount, optional F-mount.
Camera Head Size: 4.15"W x 3.60"H x 1.67"D (105.4 x 91.44 x 42.42mm).
Controller Board: Full size PCI 2.2 board (occupies one slot).
Cable: 5 meter length
Trigger:
-Electrical Properties TTL (5V-tolerant) compatible signal.
-User selects logical high, low, positive edge, negative edge or switch closure.
-Variable Positioning The trigger position (i.e. the number of pre- and post-trigger frames) is selectable in 1% increments between 0 and the frame capacity –1.
Frame Sync: Any number of cameras may be synchronized either to a "master" camera or to an external source. Accuracy of synchronization between cameras is within 2μ seconds.

Exposure Out: An exposure out signal is available for synchronizing a strobe or another device. This signal remains high (3.3V) while the shutter is open.

Recording Modes: Circular Buffer Records images into circular buffer until triggered, then user- selected number of post-trigger frames (from 0 to total number of frames in buffer -1) are recorded.

Multiple Session:

-Burst on Trigger.

-User-selected numbers of frames are recorded every time the camera receives a trigger until memory is full.

-Record on Trigger Records whenever the trigger signal is "true" until the memory is full.

Frame Storage:

-Standard Up to 2 GB: 1635 full frames.

-Enhanced Up to 4 GB: 3273 full frames.

-Maximum Up to 6 GB: 4912 full frames.

Playback Rates: User selectable variable playback.

Multi-Camera Control: Up to four cameras may be operated on one PC.

Operator Environment: Point & click environment for Windows 2000 and Windows NT 4.0 SP6.

Reticle: Pixel coordinates of the reticle position are always displayed on screen.

Analysis Features:

-Microsoft Excel compatible features including angular, linear, velocity and rotational measurements.

-Track multiple points over multiple frames.

-A lens calculator tool that computes lens selection, depth of field, magnification factor and motion blur.

File Formats: AVI, BMP, JPEG, TIFF

PC Minimum Platform: Celeron 800 MHz, 1024 x 768 display resolution, 128 MB RAM, 10 GB Hard Drive, 64 MB video RAM, CD-R Drive, 3.3V PCI 2.2 compliant motherboard, at least one empty full-length PCI slot, Windows NT or Windows 2000. Note: Specifications are subject to change.

Worlwide Sales and Support

Americas
tel: +1-800-462-4307
tel: +1-858-481-8182
sales@redlake.com

Asia Pacific
tel: +65-6293-4758
salesASPAC@redlake.com

Japan
tel: +81-3-5639-2770
salesJapan@redlake.com

Europe, Africa and Middle East
tel: +31-347-324989
salesEurope@redlake.com

Appendix F

Stress Chain Data

Photoelastic Discs

Experiment 1

Frames Per Second: 125

Angle of Platform	Angle of Chain	Difference in Angle Between the Platform and Chain	Number of beads thick	Length of Chain (inches)
18	90	72	4	2
18	100	82	3	1.5
18	100	82	4	2
18	98	80	3	1.5
18	94	76	4	2
18	95	77	4	2
18	95	77	3	1.5
18	80	62	3	1.5
18	98	80	2	1

Experiment 2

Frames Per Second: 200

Angle of Platform	Angle of Chain	Difference in Angle Between the Platform and Chain	Number of beads thick	Length of Chain (inches)
28	94	66	4	2
28	86	58	3	1.5
28	100	72	4	2
28	70	42	5	2.5
28	98	70	4	2
28	82	54	3	1.5
28	97	69	3	1.5
28	86	58	3	1.5
28	86	58	4	2
28	97	69	4	2

Experiment 3

Frames Per Second: 250

Angle of Platform	Angle of Chain	Difference in Angle Between the Platform and Chain	Number of beads thick	Length of Chain (inches)
30	98	68	3	1.5
30	100	70	4	2
30	85	55	5	2.5
30	85	55	4	2
30	80	50	4	2
30	95	65	3	1.5
30	82	52	3	1.5
30	75	45	4	2

30	82	52	3	1.5
30	92	62	3	1.5

Experiment 4
Frames Per Second: 250

Angle of Platform	Angle of Chain	Difference in Angle Between the Platform and Chain	Number of beads thick	Length of Chain (inches)
22	84	62	5	2.5
22	97	75	3	1.5
22	98	76	4	2
22	80	58	4	2
22	83	61	3	1.5
22	88	66	5	2.5
22	93	71	3	1.5
22	97	75	3	1.5
22	87	65	4	2
22	84	62	5	2.5
22	82	60	4	2
22	82	60	4	2
22	98	76	3	1.5
22	86	64	3	1.5

Experiment 5
Frames Per Second: 250

Angle of Platform	Angle of Chain	Difference in Angle Between the Platform and Chain	Number of beads thick	Length of Chain (inches)
22	100	78	4	2
22	86	64	3	1.5
22	94	72	4	2
22	86	64	5	2.5
22	83	61	4	2
22	88	66	5	2.5
22	86	64	6	3
22	76	54	4	2
22	88	66	4	2
22	87	65	4	2

Table F.1: Data collected on stress chain orientation from photoelastic disc experiments.

Bibliography

Blong R. J., 1984, *Volcanic Hazards: A Sourcebook on the Effects of Eruptions*. Academic Press, Orlando, Florida.

Iverson R., Schilling S. and Vallance J., 1998, Objective delineation of lahar-inundation hazard zones. *Geological Society of American Bulletin*, 110(8): 972-984.

Lipman P. and Mullineaux D., 1982, The 1980 Eruptions of Mount St. Helens, Washington. *Geologic Survey Professional Paper* 1250, 1-844.

Jaeger H., Nagel S. and Behringer R., 1996 A, Granular solids, liquids and gases. *Rev. of Mod. Phys.*, 68(4): 1259-1273.

Jaeger H., Nagel S. and Behringer R., 1996 B, The physics of granular materials. *Phys. Today*, 49: 32-38.

Behringer R., Jaeger H. and Nagel S., 1999, Introduction to the focus issue on granular materials. *Chaos*, 9(3): 509-510.

Daerr A., 2001, Dynamical equilibrium of avalanches on a rough plane. *Phys. of fluids*, 13(7): 2115-2124.

Tischer M., Bursik M. and Pitman B., 2001, Kinematics of sand avalanches using particle-image velocimetry. *J. of Sed. Research*, 71(3): 355-364.

Savage S.B. and Hutter K., 1989, The motion of a finite mass of granular material down a rough incline. *J. Fluid Mech.*, 199: 177-215.

Gray J., Wieland M. and Hutter K., 1999, Gravity-driven free surface flow of granular avalanches over complex basal topography. *Proc. R. Soc. Lond. A*, 455: 1841-1874.

Wieland M., Gray J. and Hutter K., 1999, Channelized free-surface flow of cohesionless granular avalanches in a chute with shallow lateral curvature. *J. Fluid Mech.*, 392: 73-100.

Greve R., Koch T. and Hutter K., 1994, Unconfined flow of granular avalanches along a partly curved surface. 1. Theory. *Proc. R. Soc. Lond. A*, 445: 399-413.

Koch T., Greve R. and Hutter K., 1994, Unconfined flow of granular avalanches along a partly curved surface. 2. Experiments and numerical computations. *Proc. R. Soc. Lond. A*, 445: 415-435.

Hutter K. and Koch T., 1991, Motion of a granular avalanche in an exponentially curved chute: experiments and theoretical predictions. *Phil. Trans. R. Soc. Lond. A,* 334(1633): 93-138.

Pouliquen O. and Renaut N., 1996, Onset of granular flows on an inclined rough surface: dilatancy effects. *J. Phys. Paris II*, 6: 923-935.

Daerr A. and Douady S., 1999, Two types of avalanche behaviour in granular media. *Nature*, 399: 241-243.

Pouliquen O. and Forterre Y., 2001, Friction law for dense granular flows: application to the motion of a mass down a rough inclined plane. *J. Fluid Mech.*, 453: 133-151.

Denlinger R. and Iverson R., 2001, Flow of variably fluidized granular masses across three-dimensional terrain; 2, numerical predictions and experimental tests. Journal of Geophysical Research, B, 106(1): 553-566.

Berger M. and Colella P., 1989, Local adaptive mesh refinement for shock hydrodynamics. *Journal of Computer Physics*, 82: 64-84.

Davis S., 1988, Simplified second-order godunov-type methods. *SIAM Journal on Scientific and Statistical Computing*, 9: 445-473.

Patra A., Bauer A., Nichita C., Pitman E., Sheridan M., Bursik M., Rupp B., Webb A., Stinton A., Namikawa L. and Renschler C., 2003, Parallel Adaptive Numerical Simulation of Dry Avalanches over Natural Terrain. Submitted, *J. Volcanology and Geothermal Research*.

Pitman E., Nichita C., Patra A., Bauer A, Sheridan M. and Busik M., 2003, Computing granular avalanches and landslides. *Physics of Fluids*, 15(12): 3638-3646.

Papa M., Egashira S. and Itoh T., 2003, Critical conditions of bed sediment entrainment due to debris flow. *Geophysical Research Abstracts*, 5, 09673.

Nichita C., Bursik M., Patra A., Pitman E., Rupp B. and Webb A., 2004, A model of erosional volcanic granular flows. *Submitted, Bulletin of Vocanology*.

Geng J., Behringer R., Reydellet G. and Clement E., 2003, Greens Fuction Measurements in 2D Granular Materials. *Physica D,* 182: 274-303.